

# NAVAL POSTGRADUATE SCHOOL

## Monterey, California

AD-A237 681



# THESIS

INSTRUMENTATION REQUIREMENTS FOR TREE EFFECTS  
DATA COLLECTION AT THE  
NAVAL POSTGRADUATE SCHOOL FLASH X-RAY FACILITY

by

Dale Galarowicz

June 1990

Thesis Advisor

X. K. Maruyama

Approved for public release; distribution is unlimited.

91-03270



unclassified

SECURITY CLASSIFICATION OF THIS PAGE

REPORT DOCUMENTATION PAGE				Form Approved OMB No 0704-0188	
1a REPORT SECURITY CLASSIFICATION unclassified			1b RESTRICTIVE MARKINGS		
2a SECURITY CLASSIFICATION AUTHORITY			3 DISTRIBUTION AVAILABILITY OF REPORT Approved for public release; distribution unlimited		
2b DECLASSIFICATION/DOWNGRADING SCHEDULE					
4 PERFORMING ORGANIZATION REPORT NUMBER(S)			5 MONITORING ORGANIZATION REPORT NUMBER(S)		
6a NAME OF PERFORMING ORGANIZATION Naval Postgraduate School		6b OFFICE SYMBOL (If applicable) 32	7a NAME OF MONITORING ORGANIZATION Naval Postgraduate School		
6c ADDRESS (City, State, and ZIP Code) Monterey, CA 93943-5000			7b ADDRESS (City, State, and ZIP Code) Monterey, CA 93943-5000		
8a NAME OF FUNDING/SPONSORING ORGANIZATION		8b OFFICE SYMBOL (If applicable)	9 PROCUREMENT INSTRUMENT IDENTIFICATION NUMBER		
8c ADDRESS (City, State, and ZIP Code)			10 SOURCE OF FUNDING NUMBERS		
			PROGRAM ELEMENT NO	PROJECT NO	TASK NO
11 TITLE (Include Security Classification) INSTRUMENTATION REQUIREMENTS FOR TREE EFFECTS DATA COLLECTION AT THE NAVAL POSTGRADUATE SCHOOL FLASH X-RAY FACILITY					
12 PERSONAL AUTHOR(S) Dale Galarowicz					
13a TYPE OF REPORT Master's Thesis		13b TIME COVERED FROM _____ TO _____	14 DATE OF REPORT (Year Month Day) June 1990		15 PAGE COUNT 118
16 SUPPLEMENTARY NOTATION The views expressed in this thesis are those of the author and do not reflect the official policy or position of the Department of Defense or the U.S. Government.					
17 COSATI CODES			18 SUBJECT TERMS (Continue on reverse if necessary and identify by block number)  EMP. IEMP, Flash X-ray instrumentation		
FIELD	GROUP	SUB-GROUP			
19 ABSTRACT (Continue on reverse if necessary and identify by block number)  The collection of photon-induced transient radiation effects on electronics (TREE) data in a pulsed X-ray facility is hampered by severe electrical noise created by the pulse generation process. This thesis presents suitable techniques for data collection and evaluation when using the Pulserad Model 112A pulsed X-ray generator installed in the Naval Postgraduate School Flash X-ray facility.  The TREE of wafer scale integrated devices is of primary concern to researchers at this time; therefore, instrumentation development was based primarily on the needs dictated by these devices. A brief description of the current status of wafer scale integrated devices is presented along with some basic TREE data collected on these devices.					
20 DISTRIBUTION AVAILABILITY OF ABSTRACT <input checked="" type="checkbox"/> UNCLASSIFIED/UNLIMITED <input type="checkbox"/> SAME AS REF <input type="checkbox"/> DTIC USERS			21 ABSTRACT SECURITY CLASSIFICATION unclassified		
22a NAME OF RESPONSIBLE INDIVIDUAL X. K. Maruyama			22b TELEPHONE (Include Area Code) (408) 646-2431		22c OFFICE SYMBOL PH/Mx

DD Form 1473, JUN 86

Previous editions are obsolete

S/N 0102-LF-014-6603

i

unclassified

Approved for public release; distribution is unlimited.

Instrumentation Requirements for TREE Effects Data Collection  
at the Naval Postgraduate School Flash X-Ray Facility

by

Dale Galarowicz  
Electrical Engineer, Physics Department, Naval Postgraduate School  
B.S.E.E., Naval Postgraduate School, 1988

Submitted in partial fulfillment of the  
requirements for the degree of


MASTER OF SCIENCE IN ELECTRICAL ENGINEERING

from the

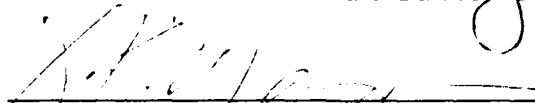
NAVAL POSTGRADUATE SCHOOL

June 1990

Author:

  
Dale Galarowicz

Approved by:

  
X. K. Maruyama, Thesis Advisor



S. N. Michael, Second Reader



J. P. Powers, Chairman  
Department of Electrical and Computer Engineering

## ABSTRACT

The collection of photon-induced transient radiation effects on electronics (TREE) data in a pulsed X-ray facility is hampered by severe electrical noise created by the pulse generation process. This thesis presents suitable techniques for data collection and evaluation when using the Pulserad Model 112A pulsed X-ray generator installed in the Naval Postgraduate School Flash X-ray facility.

The TREE of wafer scale integrated devices is of primary concern to researchers at this time; therefore, instrumentation development was based primarily on the needs dictated by these devices. A brief description of the current status of wafer scale integrated devices is presented along with some basic TREE data collected on these devices.



Accession For	
ATIS GRAB	<input checked="" type="checkbox"/>
DTIC Tab	<input type="checkbox"/>
Downloaded	<input type="checkbox"/>
Justification	
By	
Distribution	
Availability Codes	
Avail and/or	
Dist Special	
A-1	

## TABLE OF CONTENTS

I.	INTRODUCTION.....	1
II.	CURRENT STATUS OF HYBRID WAFER SCALE INTEGRATED TECHNOLOGY.....	3
III.	THE ELECTROMAGNETIC PULSE AND ITS EFFECTS.....	9
	A. THE GENERATION OF AN ELECTROMAGNETIC PULSE.....	12
IV.	THE FLASH X-RAY GENERATOR AS A PHOTON SOURCE FOR INDUCED ELECTROMAGNETIC PULSE EXPERIMENTS.....	16
	A. NAVAL POSTGRADUATE SCHOOL (NPS) FLASH X-RAY (FXR) FACILITY.....	18
	B. ELECTRICAL NOISE PROBLEMS ASSOCIATED WITH THE NPS FXR FACILITY.....	21
	C. ISOLATION OF NOISE SOURCES IN THE NPS FXR FACILITY.....	25
V.	PREDICTION OF PHOTON INDUCED ELECTRON YIELDS FOR WAFER SCALE INTEGRATED DEVICES.....	32
VI.	INSTRUMENTATION REQUIREMENTS FOR THE MEASUREMENT OF IEMP IN WAFER SCALE INTEGRATED DEVICES AT THE NPS FXR FACILITY.....	45
	A. LIMITATIONS OF FIBER OPTIC AND DIFFERENTIAL DATA LINKS.....	52
	B. THE DIFFERENTIAL DATA COLLECTION METHOD AS APPLIED TO THE NPS FXR FACILITY.....	56

VII.	INTERPRETATION OF RESULTS AND EFFECTS DURING IEMP TESTING.....	72
A.	DIFFERENTIATING BETWEEN PHOTON EFFECTS AND EMP EFFECTS.....	79
B.	REDUCTION OF PHOTON EFFECTS OF EXTRANEIOUS OBJECTS DURING IEMP TESTING.....	83
VIII.	CONCLUSIONS AND RECOMMENDATIONS .....	93
	APPENDIX A – Characterization of NPS FXR Data Link.....	94
	APPENDIX B – Condensed Operating Procedures for NPS FXR Differential Data Link.....	102
	LIST OF REFERENCES.....	105
	INITIAL DISTRIBUTION LIST.....	107

## LIST OF DEFINITIONS AND ABBREVIATIONS

Balun	Balanced to unbalanced
CMRR	Common mode rejection ratio
DCS	Digitizing camera system
EMP	Electromagnetic pulse
Fluence	The transfer of energy (in ergs, joules, or calories) across a unit of area (cm <sup>2</sup> )
FWHM	Full width half maximum
FXR	Flash X-Ray
IC	Integrated circuit
IEMP	(Photon) induced electromagnetic pulse
LLNL	Lawrence Livermore National Laboratory
MLC	Multilayer ceramic
NPS	Naval Postgraduate School
PCB	Printed circuit board
R	Roentgens
Rad	Radiation absorbed dose
Rad(Si)	Radiation absorbed dose in silicon
RFI	Radio frequency interference
SiPCB	Silicon printed circuit board
SNR	Signal to noise ratio
Triax Cable	A transmission line with a single center conductor and two separate concentric shields
TREE	Transient radiation effects on electronics
Tri-filar	Three separate insulated conductors uniformly twisted together

## ACKNOWLEDGEMENT

The information presented in this thesis was the result of the combined talents of a number of individuals. The assistance provided by my advisors, Drs. X. K. Maruyama and S. N. Michael, made the experiments performed and instruments constructed possible. The previous work of Renee B. Pietruszka [Ref. 10], and the assistance of Mr. Bernie Bernstein and Mr. Richard Mendosa of Physics International Company provided the critical information necessary for characterizing the Model 112A Pulsed X-ray Generator.

The combined contributions of Mr. Herb Bracewell, Dr. Nicholas Colella, Dr. Joseph Kimbrough and Dr. Richard W. Adler made the collection of wafer scale device data a possibility.

Special thanks are also due to Mr. Donald D. Snyder, Mr. Harold M. Rietdyk, and Mr. George B. Jaksha of the Physics Department of the Naval Postgraduate School, Monterey, CA, without whose help, technical assistance, and advice, this work would not have been possible.



## I. INTRODUCTION

The pulsed X-ray generator first came into use for the testing of electronic components in the early 1960's. Since then much work has been done in the field of pulsed power generation, primarily by Physics International Company, Ion Physics Corporation, Maxwell Laboratories, Cornell University, and Sandia National Laboratories.

To accommodate the growing demand for pulsed X-ray testing, many new facilities have sprung up in recent years. The newly acquired Flash X-ray test facility at the Naval Postgraduate School serves the needs of several government and civilian agencies engaging in electromagnetic pulse effects testing and evaluation.

The purpose of this study was to investigate and characterize appropriate methods for the collection of photon-induced electromagnetic pulse effects on small-scale electronic components, with an emphasis on wafer-scale integrated devices. Only a minimal amount of TREE testing experience is required on the part of the reader.

Chapter II provides a brief description of the current status of wafer-scale integrated devices. Chapters III and IV discuss the electromagnetic pulse, its simulation with the use of a flash X-ray generator, and the electrical noise problems present in a typical flash X-ray facility. Chapter V discusses methods of yield predictions for typical testing configurations. Chapter VI describes in detail the instrumentation requirements and construction methods suitable for use in TREE testing, and, lastly, Chapter VII interprets tests results and effects.

All research performed for this study took place at the Naval Postgraduate School Flash X-ray facility utilizing a Physics International Model 112A Pulsed X-ray generator.

## II. CURRENT STATUS OF HYBRID WAFER SCALE INTEGRATED TECHNOLOGY

Integrated circuit (IC) technology has experienced dynamic growth in recent years, with a continuing trend toward higher speed and higher density packaging. In many cases the performance of modern systems is no longer limited by the integrated devices themselves, but rather by the methods of interconnection of these devices for multiple IC systems.

The use of the conventional epoxy glass multilayer printed circuit board (PCB) has reached the limits of technological feasibility as far as density and operating speed are concerned, so new methods have been devised to enhance overall system performance. Among these are the Multilayer Ceramic (MLC) and the silicon printed circuit board (SiPCB) technologies.

The MLC technology, although far superior to conventional PCB methods, has limitations due to the manufacturing processes. These limitations restrict the minimum geometry of interconnects to rather coarse dimensions (250  $\mu\text{m}$  widths) requiring large numbers of metal layers (up to 33) to accommodate high density IC's. Other problems include a thermal expansion mismatch between the silicon and alumina substrate, low propagation speeds due to the large dielectric constant of the alumina, and a substantial thermal resistance caused by the thick ceramic substrate.

The use of SiPCB technology can provide a high density of interconnects with a minimum of metalization layers (3 or 4 typical) and can also circumvent other problems associated with MLC technologies. SiPCB's possess exceptional mechanical properties with virtually no noticeable thermal stresses (due to the thermal expansion match between the IC's and the SiPCB), and liquid-cooled

versions have demonstrated an ability to dissipate more than 1000 watts/cm<sup>2</sup> of heat while maintaining normal IC operating temperatures.

Figure 2.1 shows a possible layout of a SiPCB. The SiPCB performs the function of a conventional PCB, except on the wafer scale (wafer scale distances of up to 20 cm are possible at this time). [Refs. 1,2,3]

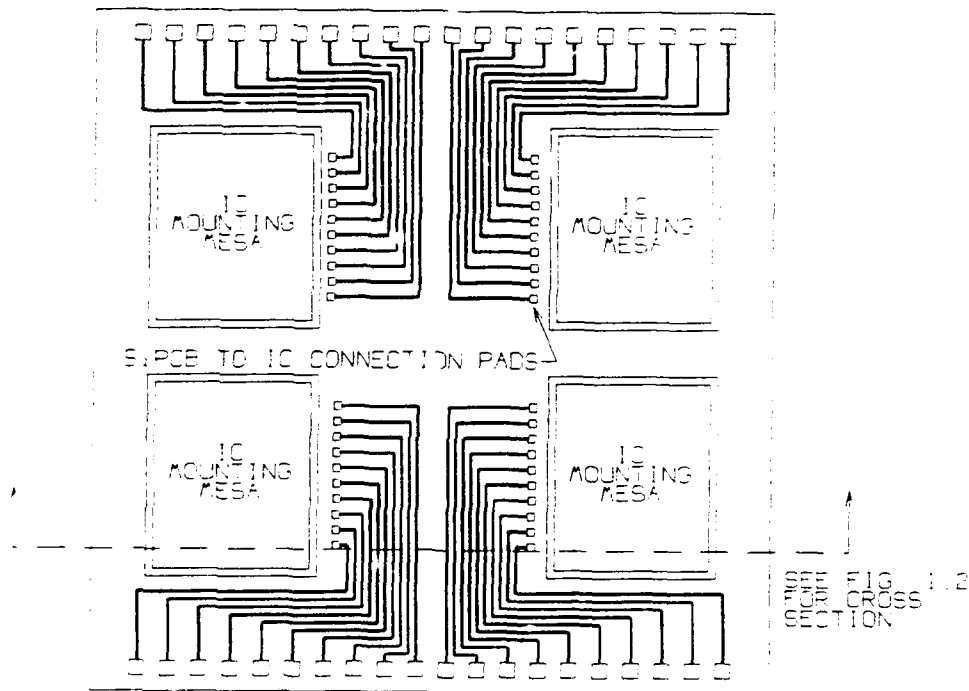


Figure 2.1 A Hypothetical SiPCB with 4 Mounting Mesas  
(Prior to IC Attachment)

Integrated circuits are bonded to the SiPCB with conventional interconnecting metallurgy techniques (Au/Ti:W/SiO<sub>2</sub> or Cu/polymide are examples). As shown in the cross-section of Figure 2.2, the SiPCB, having previously been fabricated with

appropriate interconnecting traces for the circuit configuration being used, can now be connected to the attached IC's.

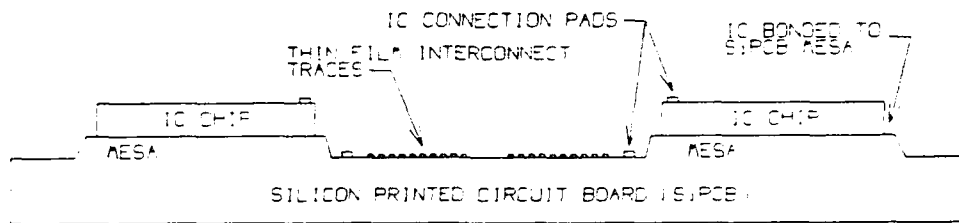


Figure 2.2 Cross Section of the SiPCB of Figure 2.1 with IC's Mounted, Ready for Microgrinding and Laser Defined Interconnection

There are a number of methods currently in use to connect the IC conductor pads to the interconnects on the SiPCB. The conventional techniques used to date involve welding or soldering of the IC pads directly by mounting the chip with the IC substrate away from the SiPCB (the so-called Flip Chip technique), or by the use of microscopic wires welded between the IC and the SiPCB (wire bonding). Both of these methods have serious limitations: for the Flip Chip, high thermal resistance between the IC and the SiPCB limits power dissipation; and, for wire bonding, the relatively high inductance of the wire interconnects reduces high speed operation.

A more novel technique, currently being developed at the Lawrence Livermore National Laboratory (LLNL), entails the deposition of thin film interconnecting patterns down the edges of the IC using laser etching techniques. This technology has been shown to have good electrical properties, high interconnect density (1600

connections on a 1 cm<sup>2</sup> IC), mechanical integrity, low inductance and low thermal resistance between the SiPCB and the heat sinking device.

Figure 2.3 shows the cross section of Figure 2.2 after the edges of the IC and SiPCB have been contoured with a microgrinder and laser-defined interconnects have been etched to connect the IC's to the SiPCB.

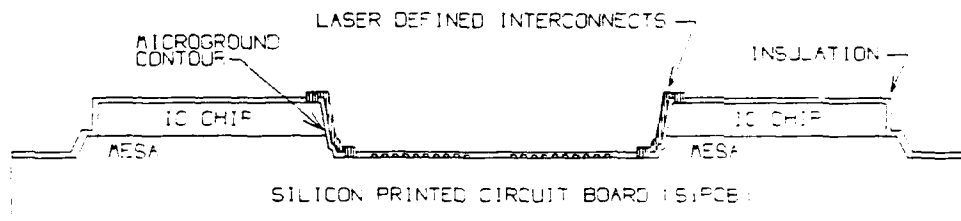


Figure 2.3 SiPCB After Microgrinding, Insulation Deposition, and Laser Defined Interconnection of IC Chip

To date, research conducted at LLNL has been directed towards basic development, design, and evaluation of test samples mating custom-made and commercially-available IC's with SiPCB's, including modules utilizing 10 static ram memory chips (64K National Semiconductor NVC 63Q64) (Figure 2.4), temperature sensors (Figure 2.5), strain gauges, and various small scale integrated devices.

Since the SiPCB technology lends itself readily to military and space systems, additional data is required with respect to nuclear effects. The research addressed in this thesis examines the problems associated with the collection of data during electromagnetic pulse (EMP) testing of the SiPCB interconnects and substrate. This data, in conjunction with data collected during underground nuclear tests, will

provide the additional information necessary to characterize SiPCB assemblies with regard to projected nuclear threats. For a more detailed discussion on the current status of SiPCB technology, refer to the three sources of information used in this brief description [Refs. 1,2,3].

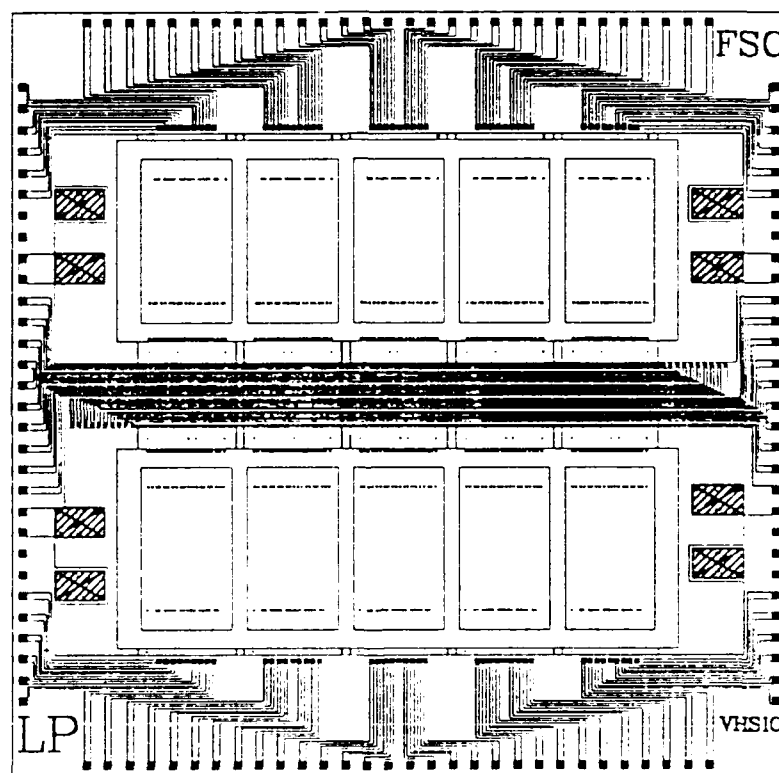


Figure 2.4 First-Level-Metal Pattern of the Multichip Memory Module.  
Each Side is 4.58 cm Long. [Ref. 3:Fig. 1.3-1:p. 14]

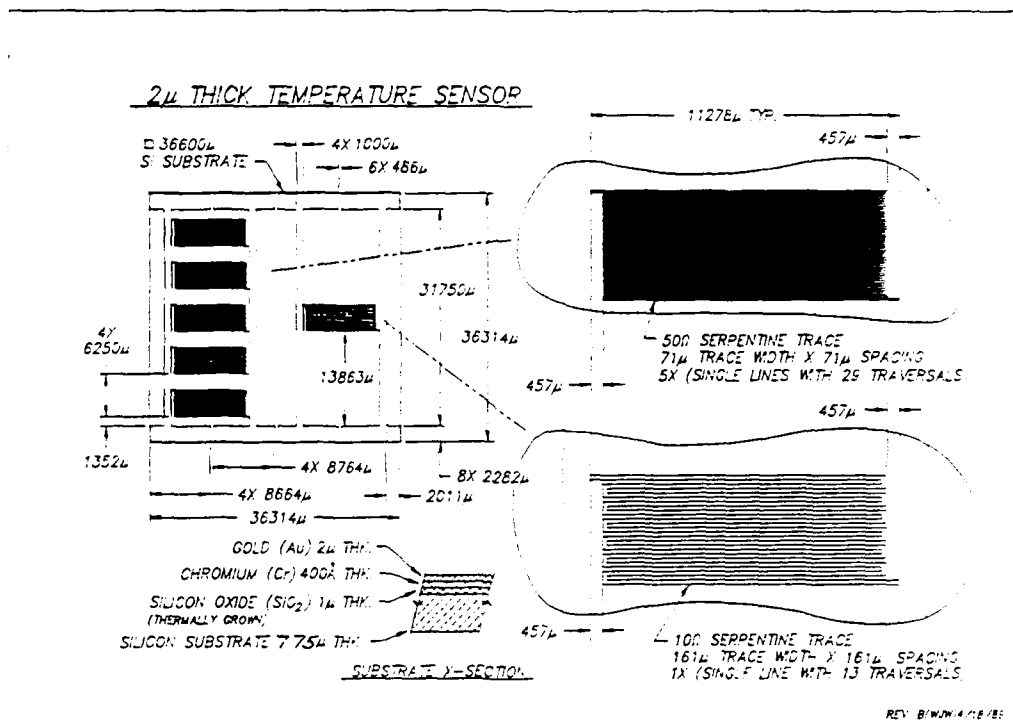


Figure 2.5 Temperature Sensor Used for SiPCB Environment Tests  
[Engineering Drawing – Courtesy Joe Kimbrough, LLNL]



### III. THE ELECTROMAGNETIC PULSE AND ITS EFFECTS

The generation of an EMP by the detonation of a high explosive chemical charge is a phenomena that has been known for some time, so the generation of a similar pulse from the detonation of a thermonuclear device was anticipated prior to the initial nuclear tests of the 1940's [Ref. 4:p. 514]. During atmospheric nuclear tests in the early 1950's, unexpected failures of electronic equipment led investigators to suspect that the EMP due to nuclear effects was a far more serious problem than that generated by chemical explosions. Following the Johnston Island high altitude detonation of 1962, a simultaneous failure of 30 series-connected street light loops on the Hawaiian island of Oahu, approximately 800 miles from the test site, along with numerous burglar alarm and circuit breaker failures on power distribution lines in Honolulu confirmed the potential for damage to even insensitive electrical equipment in the face of a nuclear-generated EMP. [Ref. 4:p. 514, 523]

Since that time, much research has been done to develop methods to predict the EMP effects of nuclear detonations, including the field strengths and the extent of the damage regions. Figure 3.1 shows the effects of a high altitude nuclear explosion above the surface of the earth. The deposition region, which is the source of the EMP, is formed by the interaction of gamma and X-rays with air molecules. This region, to a first approximation, is circular in shape with a thickness of approximately 50 miles at ground zero, tapering at the edges, with a mean altitude of 30 miles. The EMP generated is relatively uniform between the deposition region and the earth with a variation of field strength of not more than a factor of two throughout the entire region. [Ref. 4:pp. 518-519]

For high altitude detonations the extent of the deposition region is large. As an example, a nuclear explosion of several hundred kilotons detonated 200–500 miles above the center of the United States could produce field strengths in excess of 10's of kilovolts per meter throughout the entire country, including large swaths of Canada and Mexico (Figure 3.2). [Ref. 5:p. 1–40][Ref. 6:pp. 2.14–2.16]

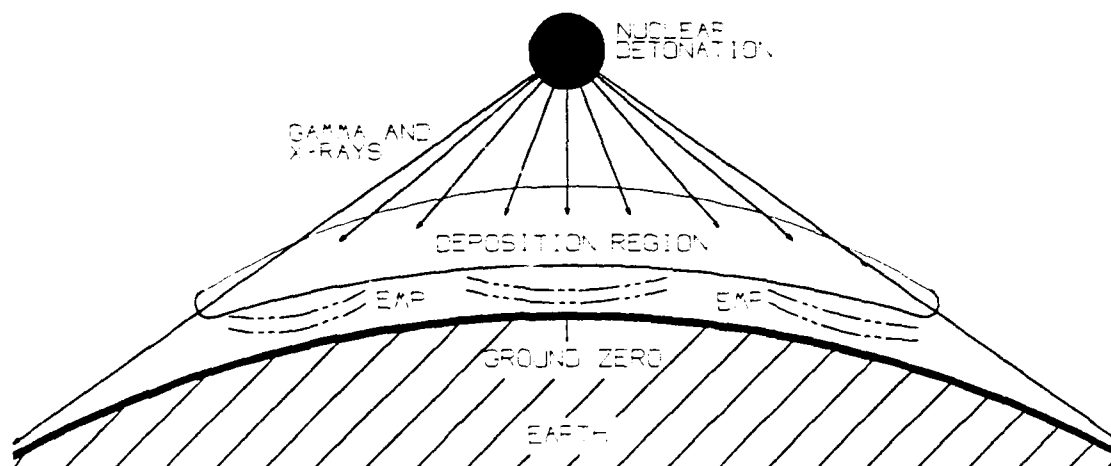


Figure 3.1 EMP Generated by a High Altitude Nuclear Detonation  
[Ref. 4:Fig. 11.13, p. 519]



Figure 3.2 EMP Ground Coverage for a Nuclear Detonation over  
the United States for Various Heights of Burst  
[Ref. 5:Fig. 1.4.2-8, p. 1-40]

This level of EMP could conceivably cause major short-term power outages, and long-term failure of numerous civilian and military computer and electronic systems, including the failure of vast segments of the telephone network in North America.

Because of these disturbing effects, military and civilian authorities alike have expended a great deal of time and energy researching the EMP effects on components, assemblies, and systems.

## A. THE GENERATION OF AN ELECTROMAGNETIC PULSE

The EMP produced by a nuclear detonation is primarily due to the prompt release of large numbers of photons and neutrons, and the subsequent interaction of these particles with the surrounding medium. The photons, being the dominate particles of interest, produce a region of high ionization around the burst point, mainly by the Compton effect [Ref. 7:pp. 160–166]. The electrons, being much lighter than the nucleus, are driven outward by the incident photons leaving the heavier, positively charged ions, creating a positive charge separation (see Figure 3.3).

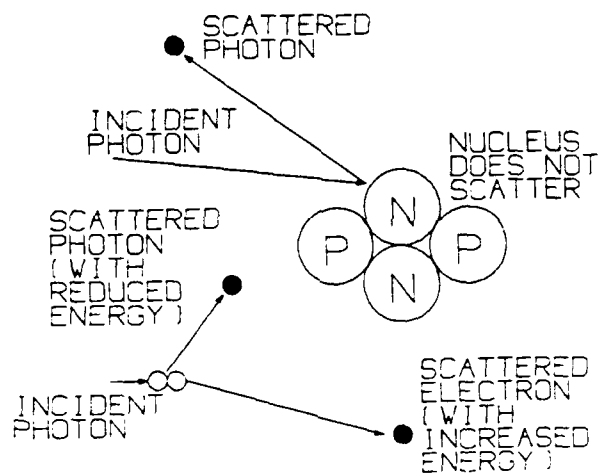


Figure 3.3 Compton Scattering

The peak magnitude of the charge separation is reached in about  $10^{-8}$  seconds, which is the approximate rise time of the EMP caused by the Compton effect [Ref. 4:p. 533], with a subsequent decay to zero which may last for a

considerably longer time. Figure 3.4 shows a typical current pulse induced in an overhead power line by the EMP resulting from a high-altitude nuclear blast. Note the fast rise time and exponential decay evident in this indirectly generated pulse.

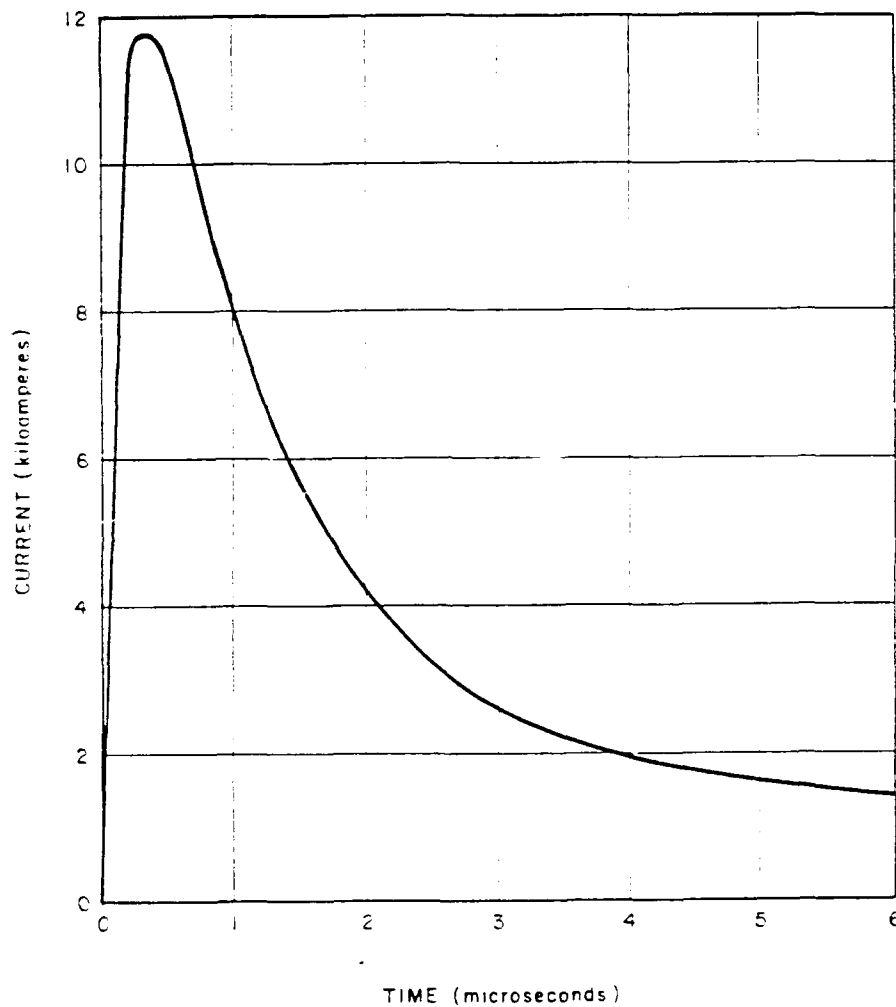


Figure 3.4 Typical Current Pulse Induced in an Overhead Power Line by the EMP Resulting from a High Altitude Nuclear Detonation [Ref. 4:Fig. 11.50, p. 530]

In addition to the EMP generated from the photon interaction with the atmosphere, there is also an EMP created by the impingement of photons on solid materials. For satellites in earth orbit, this effect becomes the dominate one, due to the rarity of the atmosphere at orbital altitudes. This locally induced field, here called the induced electromagnetic pulse (IEMP) [Ref. 8:p. 50], is created by the scattering of electrons from solid materials by the Compton effect, as was previously described.

The Compton process in solid material produces scattering in the backward as well as the forward directions. Figure 3.5a shows curves relating the forward emitted photoelectric yield per unit fluence versus photon energy, while Figure 3.5b shows the case for reverse emitted photocurrent, where fluence here is defined as the transfer of energy in calories per square centimeter. Reverse emitted photo current cannot be neglected in comparison to the forward emitted photo current.

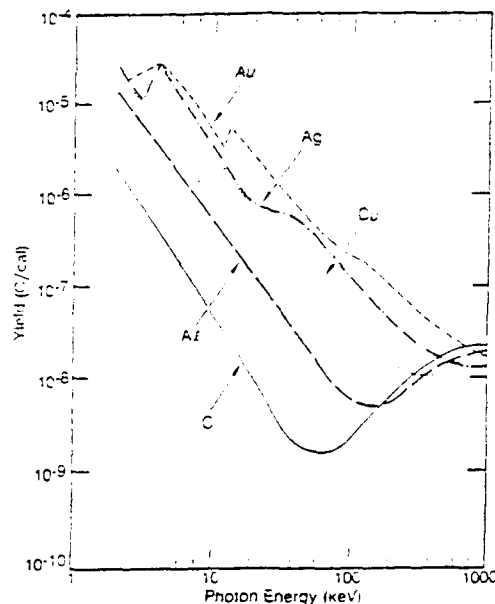


Figure 3.5a Forward  
Emitted Photoelectric Yield  
Per Unit Fluence Versus  
Photon Energy for Several  
Materials [Ref. 8:Fig. 3.3a, p. 52]

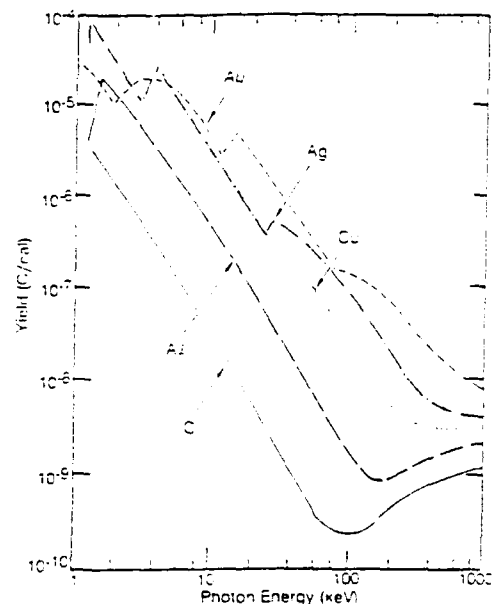


Figure 3.5b Reverse  
Emitted Photoelectric Yield  
Per Unit Fluence Versus  
Photon Energy for Several  
Materials [Ref. 8:Fig. 3.3b, p. 53]

As electrons are scattered, some of them recombine within the conductor, while some leave this parent material to become entrapped in nearby insulators, or are lost in surrounding space, depending to a large extent on the thickness of the parent material and the proximity of potential absorbing media. This creates a positive charge accumulation within the parent material. If a current path exists to a region with a neutral or negative charge density, an electric current will flow between this region and the positively-charged parent material as seen in Figure 3.6.

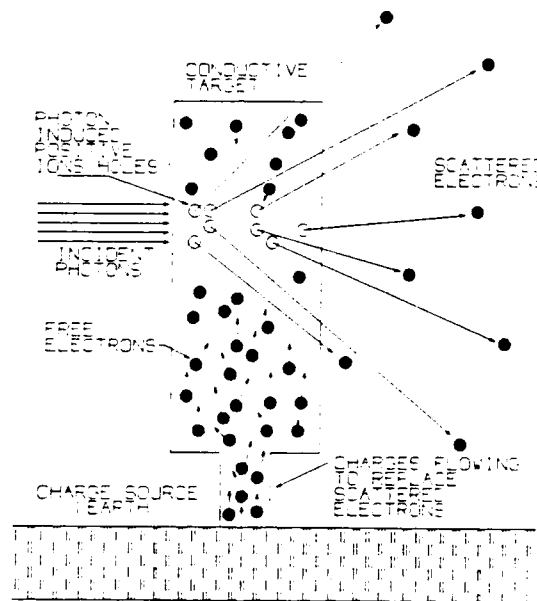


Figure 3.6 Current Pulse Generated by Photon Scattering of Electrons and Subsequent Replacement from a Charge Source

Since the rise time of the Compton effect is typically  $10^{-8}$  seconds, the pulse rise time typically will be in this neighborhood as well. However, the actual rise time, as well as the pulse fall time is greatly dependent on the conductor parameters (resistance, capacitance, inductance) and so will vary greatly from circuit to circuit.

#### IV. THE FLASH X-RAY GENERATOR AS A PHOTON SOURCE FOR INDUCED ELECTROMAGNETIC PULSE EXPERIMENTS

The use of a flash X-ray (FXR or Bremsstrahlung) generator has become the preferred method for performing IEMP testing. The Bremsstrahlung process is illustrated in Figure 4.1.

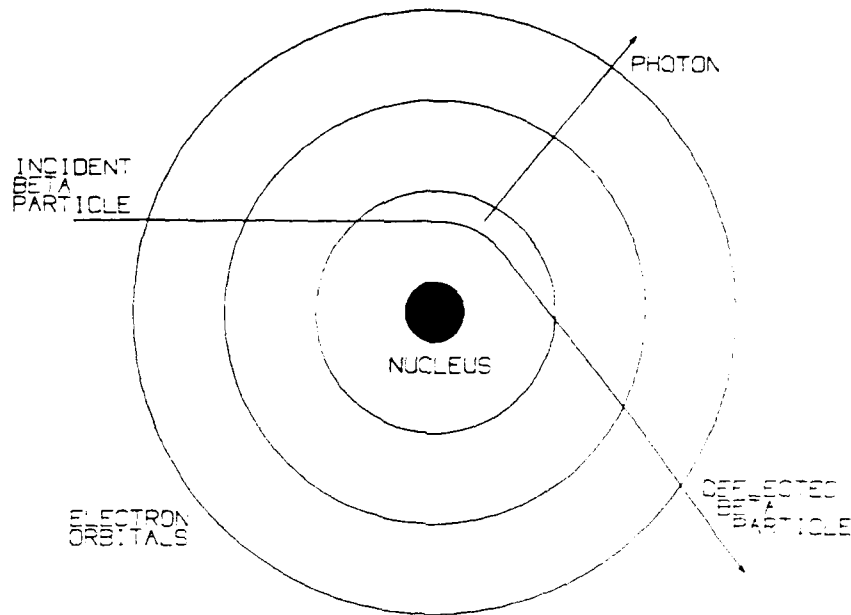


Figure 4.1 Generation of a Photon by the Bremsstrahlung Process

When a charged particle is accelerated towards a target atom, the deflection of the particle and subsequent deceleration caused by the electric field surrounding the atomic nucleus gives rise to the emission of a quantum of electromagnetic radiation. The energy of the emission (wavelength) is determined by the initial energy of the impacting particle as well as the target material properties.



Virtually all X-ray machines rely on the above phenomena for their operation. The particles used are electrons (Beta particle) and the target is a heavy element, typically tantalum. The peak energies of the electrons are usually greater than 1 MeV for practical IEMP simulations.

Figure 4.2a shows the electric field strength of a representative EMP induced by a nuclear burst, whereas Figure 4.2b indicates the cathode current for the NPS FXR facility (the photon emission time domain curves closely follow the cathode current curves). The rise time (time from zero to peak level) of the two pulses are sufficiently similar to allow the use of the FXR facility for simulation of the IEMP due to a nuclear detonation. (Note that Figure 4.2a is a representation of EMP rather than IEMP which explains the vast difference in time scales between Figure 4.2a and Figure 4.2b.)

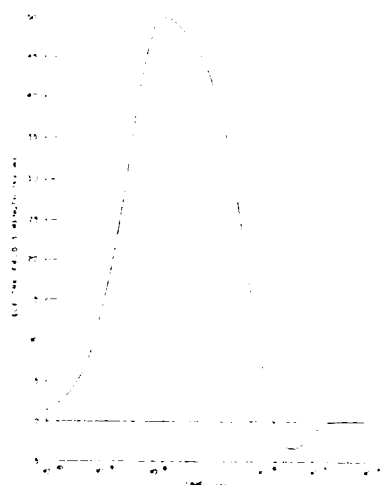


Figure 4.2a Electric Field Strength as a Function of Time for the Representative EMP [Ref. 9:p.21]

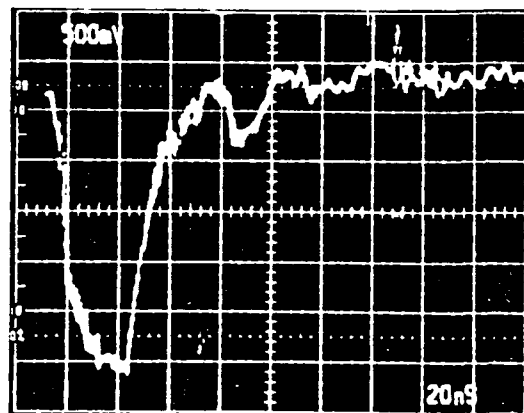


Figure 4.2b Photograph of Typical Pulserad 112A 100kV Diode Current Waveform [Ref. 10:p. 38]

Note that the nuclear induced IEMP is dependent on a great many parameters, and thus it is not unreasonable to settle for an approximation when performing EMP and IEMP testing.

#### A. NAVAL POSTGRADUATE SCHOOL (NPS) FLASH X-RAY FACILITY

The FXR facility at NPS is centered around the Model 112A Pulserad Pulsed X-ray Generator, built by Physics International of San Leandro, CA. Figure 4.3 shows a photograph of the generator face, and Table 4.1 lists its published specifications. For a more complete characterization of the Pulserad generator and its operating procedures, see references 10 and 11.

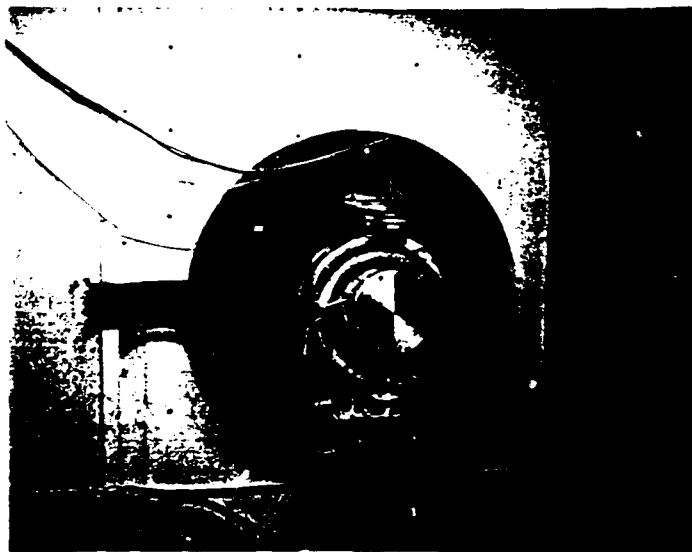


Figure 4.3 Model 112A Pulserad Flash X-Ray Generator Installation

TABLE 4.1 SYSTEMS SPECIFICATIONS OF PULSERAD  
PULSED X-RAY GENERATOR [Ref. 11:p. 3]

**Marx Generator:**

Stages:	12
Stage Capacitance:	0.05 microfarads
Output Capacitance (Total Marx):	4.7 nanofarads
Maximum Charge Voltage:	100 kV
Maximum Stored Energy:	3 kJ

**Blumlein Generator:**

Output Impedance:	43 ohms
Output Voltage:	1.7 MV
Output Pulse Width (FWHM):	20 nanoseconds

**X-ray Output:**

Dose at 0.5 Meter from Anode:	8 R
-------------------------------	-----

**Power Requirements:**

Controller:	110/220 Vac, 50/60 Hz, 500 VA max.
Vacuum System:	
Diffusion Pump:	110/220 Vac, 50/60 Hz, 500 VA max.
Fore Pump:	110/220 Vac, 50/60 Hz, 1 kVA max.
Power Supply:	220 Vac, 50/60 Hz, 500 VA max.
Oil Transfer System:	110/220 Vac, 50/60 Hz, 1 kVA max.

Referring to Figure 4.4, the salient features of the facility in its entirety can be discussed. The radiation area is enclosed in a concrete vault with the back and side walls lined with one-inch-thick steel plate (the entire building was originally designed as a jet engine test cell and is thus robustly built). All instrumentation is enclosed in a radio frequency interference (RFI) enclosure to reduce electrical noise pickup during tests. The FXR generator penetrates the concrete walls of the radiation area through a steel lined opening with the test and maintenance panels readily accessible from either end.

The layout and construction of the facility provides excellent isolation of the X-ray radiation from personnel and instrumentation. However, the incident EMP escaping from the Pulserad body presents a problem for data collection, therefore special techniques and precautions must be taken to ensure reasonable data fidelity and instrument damage protection.

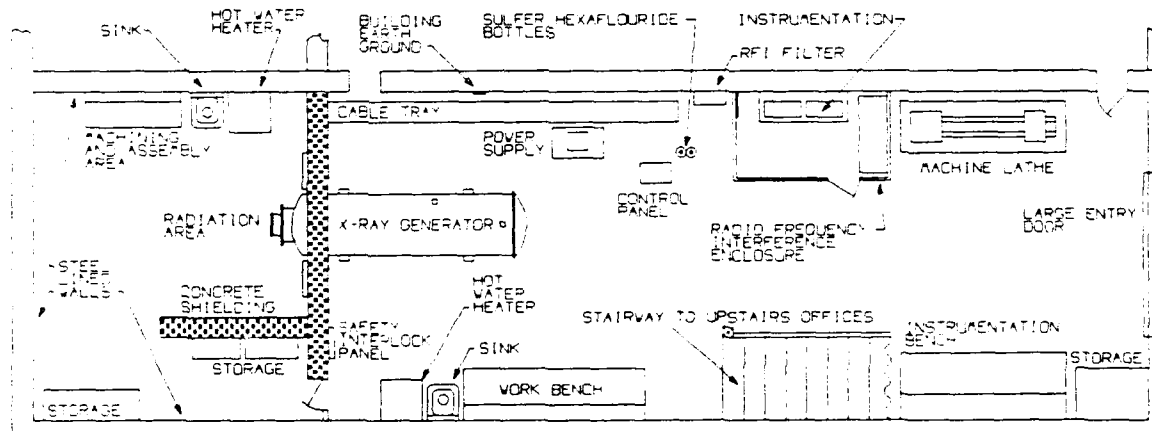


Figure 4.4 NPS FXR Facility Layout (1st Floor)

## B. ELECTRICAL NOISE PROBLEMS ASSOCIATED WITH THE NPS FXR FACILITY

The FXR generator is ideal for IEMP testing of small components and systems, however the processes involved in creating the photon beam inevitably generate a large amount of direct EMP which will interfere with normal data collection.

Figure 4.5 shows a highly simplified block diagram of the Model 112A Pulserad Flash X-ray generator indicating the pulse generation technique. The Marx Generator, which is discharged as 12 series connected 0.05 microfarad capacitors, delivers a pulse to the Blumlein Pulse generator when the pressurized spark gaps are triggered by a voltage pulse supplied from the operator "FIRE" button. Each capacitor is charged to a user-selected value, with a peak value of 100 kV. Therefore, the Marx Generator can deliver a pulse of 1.2 MV.

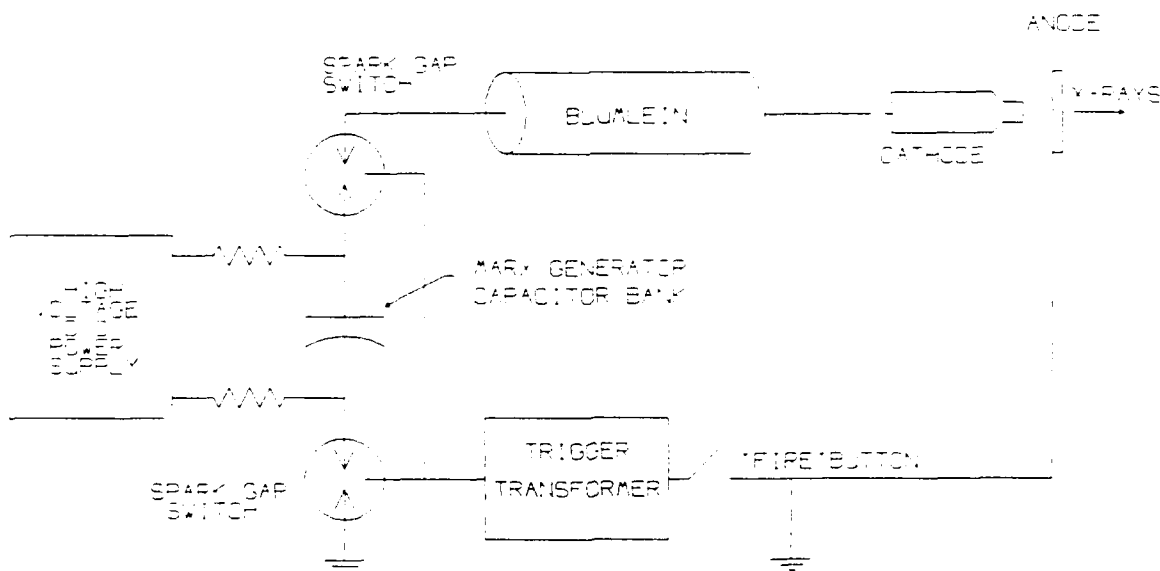


Figure 4.5 Simplified Diagram of Flash X-Ray Generator

The Blumlein Pulse generator, which is a 43 ohm resonant transmission line pulser, provides a 4:1 impedance step-up with a corresponding 2:1 voltage multiplication. The Blumlein charges up to 1.5 MV for a Marx Generator output of 1.2 MV [Ref. 11:p. 21] and provides an open-circuit output voltage of 3 MV, with an output impedance of 43 ohms. The electron accelerator impedance is 40 to 60 ohms, therefore the cathode voltage is determined, by Ohm's law, to be approximately 1.7 MV. The pulse generated by this process can be as short as 20 nanoseconds.

The peak cathode current for the above conditions is equivalent to 32 k Amps during the pulse duration, and, assuming a frequency spectrum with components beyond 12 MHz [Ref. 8:p. 144], the magnitude of the problem begins to emerge. Even with the extensive shielding on the generator itself, and a radiation resistance of the cathode being generally much less than the 50  $\Omega$  electron accelerator impedance, greatly reducing EMP radiating efficiency, there is sufficient radio frequency coupling to data links and apparatus to disrupt data collection or even to damage instruments.

In addition to the above, other sources of electrical noise are present that may create problems for the data collection apparatus. A major source of EMP is the model TX-40 high voltage trigger pulse transformer, located on top of the pulserad body near the rear access hatch. Figure 4.6 shows the relative location of the trigger transformer.

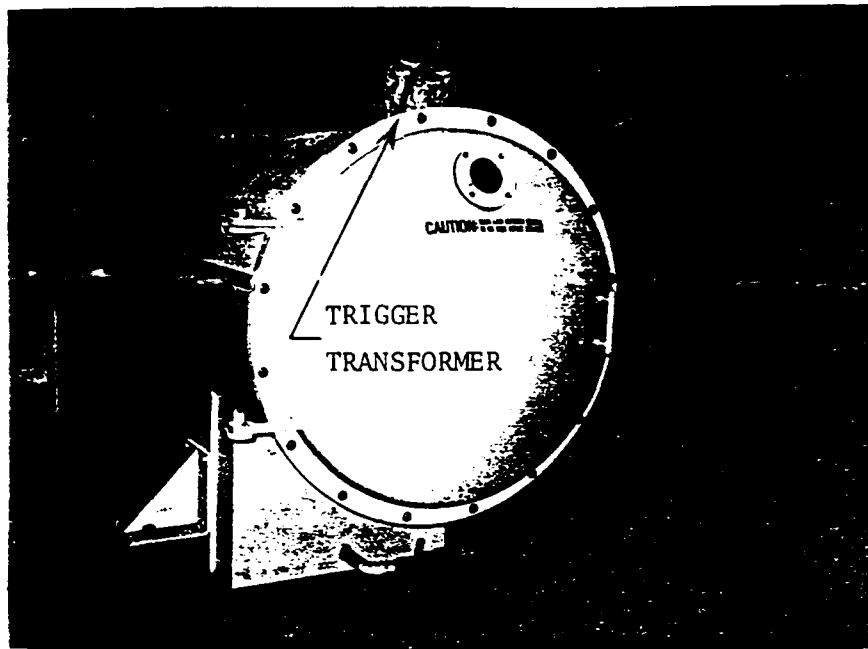


Figure 4.6 Rear View of Model 112A Pulserad Flash X-Ray Generator

Experience has shown that the trigger transformer, which is supplied unshielded by the manufacturer, must be shielded with the use of heavy aluminum foil and conductive copper tape to reduced EMP radiation. Figure 4.7 is a photograph of the trigger transformer after this shielding has been installed. Furthermore, all dc as well as ac cables connecting the transformer and pulserad body with the control console and power supply must be carefully shielded with proper earth grounds secured to the shields.

Proper grounding is also required for the RFI enclosure, and for all electrical cables entering it. The ac power lines must enter through conduits connected to the enclosure's outer surface, and shielded cables must have their shields firmly attached to the enclosure, as well, to prevent introduction of noise signals to the instruments contained therein. It should be noted that any length of conductor is

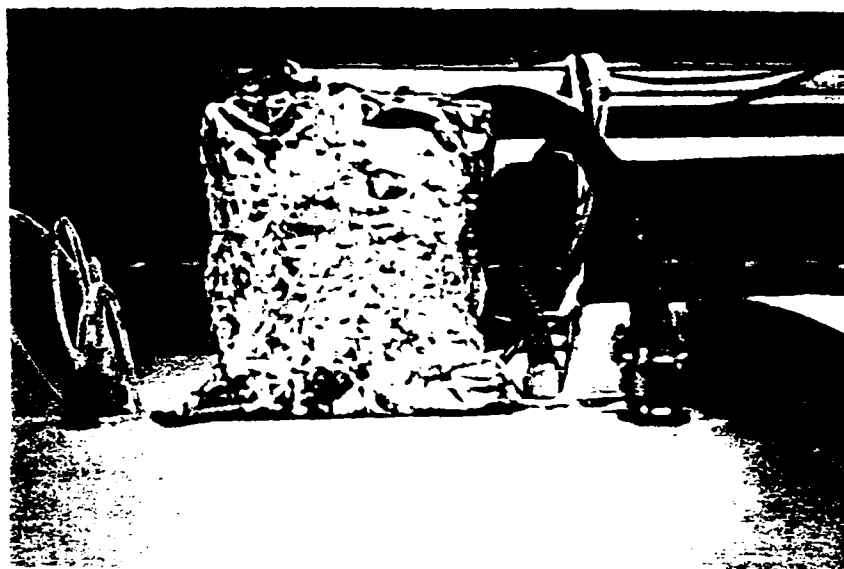


Figure 4.7 Trigger Transformer After Shielding Installation

capable of acting as a dipole antenna at some frequency, and therefore can receive and re-radiate EMP levels that could interfere with data fidelity during and after the photon-induced event.

The bonding of metallic objects to earth ground within the FXR facility should be done with braided grounding straps, as the surface area is far more important than the cross sectional area of a conductor at the radio frequencies present in typical EMP radiation (see Section VI for the explanation of skin effect and its effects on radio frequency surface currents). Furthermore, the bonding straps should be connected directly to the building earth ground pad, if possible, to facilitate a single grounding point for the elimination of ground loops. Figure 4.4 shows the location of the building earth ground and the significance of ground loops is discussed in Section VI, Figure 6.2.



The ac line power in the NPS FXR facility may also introduce electrical noise into sensitive instruments by nature of EMP pickup through electrical wiring within the building, as well as transients created by heavy equipment located in portions of the building being utilized for aeronautical engineering laboratories. These transients are removed by use of a large radio frequency interference filter, a Corom model number CDEUX400050A6, installed in the facility in such a manner as to electrically isolate the data collection apparatus from the remainder of the building. This filter is located near the RFI enclosure, as indicated in Figure 4.4.

### C. ISOLATION OF NOISE SOURCES IN THE NPS FXR FACILITY

One of the most difficult tasks encountered in data collection in any FXR facility is the isolation and elimination of noise sources. Almost imperceptible grounding or equipment problems may introduce massive noise signals into sensitive instruments making data collection impossible. Several useful methods for isolating and correcting noise sources will be presented here to assist future researchers utilizing the FXR facility.

The importance of proper earth grounds to high data fidelity was emphasized in the last section. This is by far the most common reason for the deterioration of signal-to-noise ratio on a shielded data link. Figure 4.8a shows an IEMP signal collected with the differential data link to be described in Section VI. Figure 4.8b shows a signal collected under identical conditions as Figure 4.8a, except for a poor grounding connection on one of the triaxial cables at the target. The overpowering noise displayed here is typical of that occurring due to faulty grounding conditions in the presence of strong EMP.

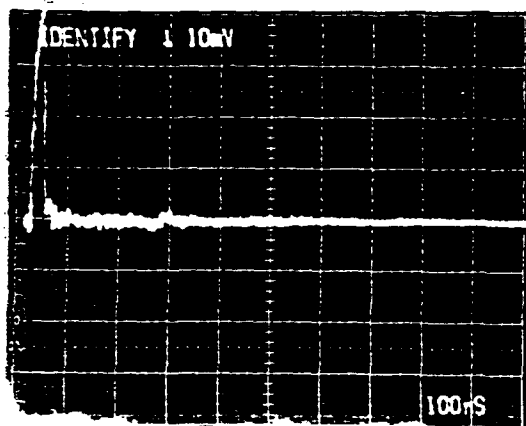


Figure 4.8a Typical IEMP Signal  
Collected with a Differential Data  
Link

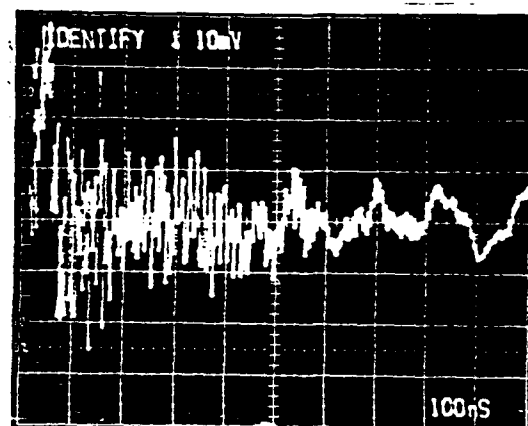


Figure 4.8b Similar Signal  
with Faulty Ground Connection  
at Target

Less obvious are the effects of noise introduced on the surfaces of shielded cables where it is only possible to ground the shields at each end of the cable. Figure 4.9a shows the differential data link with induced noise on its external shield surface. This noise was eliminated (Figure 4.9b) by the application of four ferrite filter cores on the cable assembly. Figure 4.10 depicts a split ferrite core designed

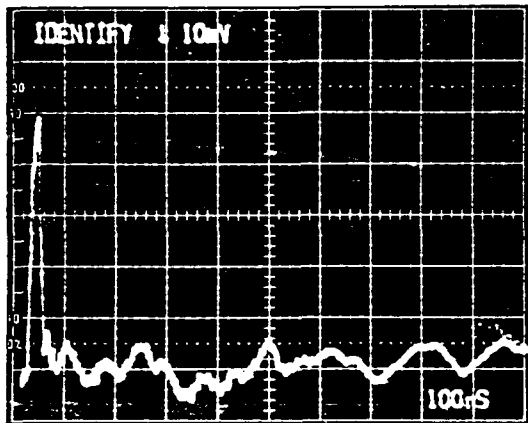


Figure 4.9a EMP Induced Noise on Differential Data Link

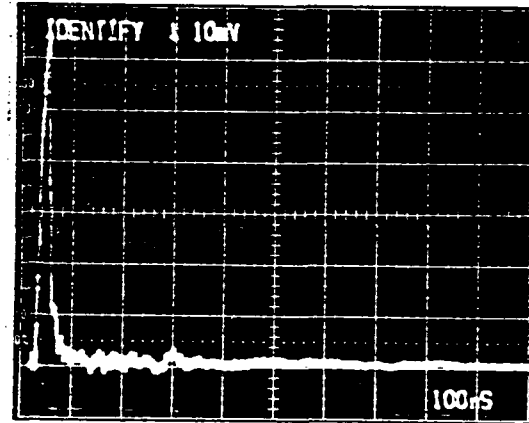


Figure 4.9b Elimination of Noise with Ferrite Cores

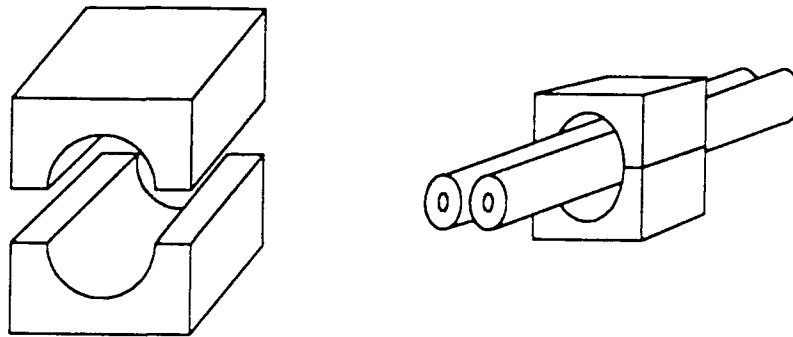


Figure 4.10 Split Ferrite Filter Core and Installation

to be installed over existing coaxial or triaxial cables to eliminate currents induced on the shield surfaces. Such cores installed on the cables will help isolate instruments from the cable surface currents by increasing the impedance presented to the common mode signal [Ref. 12:Ch. 4]. Differential mode signals will be unaffected by the filter cores due to normal transformer action.

Figure 4.11a shows the relationship between the impedance of various core filter materials and the shield current frequency. For the Amidon Associates part number BN43-151 filter core [Ref. 13:p. 72], the impedance factor indicated on the graph is approximately 5 for the 43 material. Figure 4.11b provides an equivalent circuit for the filter core installation and illustrates its effects on common-mode and differential-mode signals (Section VI.B discusses the subject in detail). It is recommended that all differential data links incorporate several BN43-151 filter cores as illustrated in Figure 4.10 to reduce shield surface currents in the NPS FXR facility. These filter cores should be installed as close as possible to the data collection instruments in the RFI enclosure.

The isolation of noise sources within the Pulserad FXR generator itself requires several special techniques. Noise sources in the generator are varied and include, among other things, poor grounding connections, leaky Marx bank resistors, and improper firing of pressurized spark gap switches. Most of the high voltage components that are used in the construction of the FXR generator are life limited, and become more troublesome with age.

As mentioned previously, the trigger pulse transformer has the potential to generate large amounts of electrical noise. This component is definitely life limited, and subject to electrical breakdown with age (accurate lifetime predictions for the model TX-40 trigger pulse transformer are unavailable from the manufacturer to

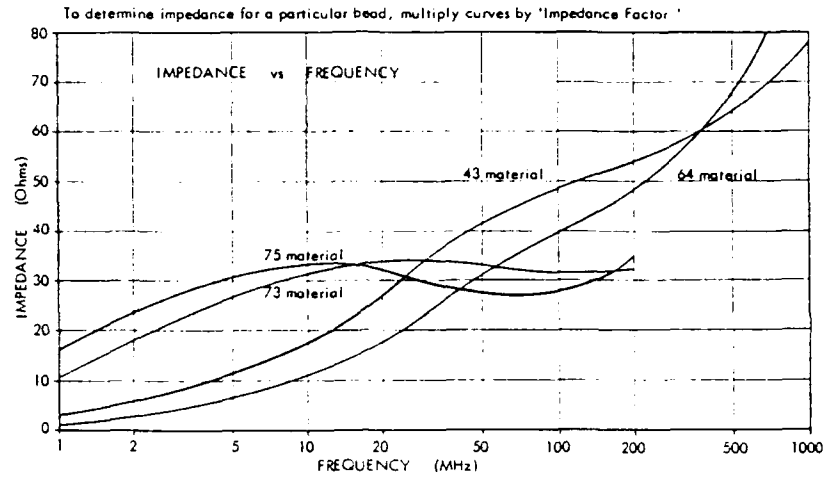


Figure 4.11a Impedance versus Frequency Curves for Various Filter Cores  
[Ref. 13:p. 50]

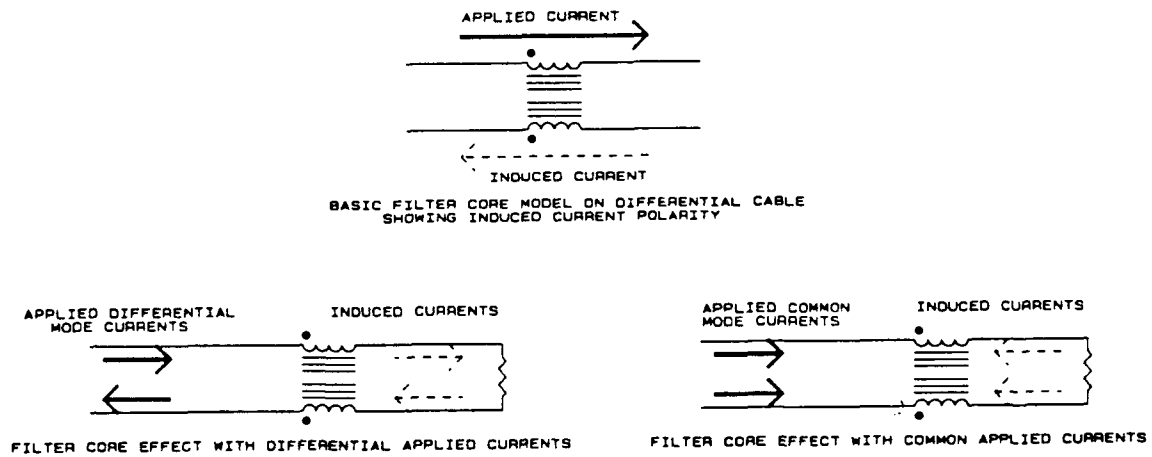


Figure 4.11b Equivalent Circuit of Filter Core Installed on Differential Data Link

date). To test the transformer's contribution to the noise environment on a particular data link, the following procedure can be used. Refer to the pulserad operations manual [Ref. 11] and the thesis of Renee B. Pietruszka [Ref. 10:pp. 13-15] as required.

1. Connect the data link and instrumentation being used for the IEMP experiment in question.
2. Do not turn on the high voltage power supply.
3. Turn on the trigger panel key switch.
4. Press the trigger button and note the electrical noise induced in the data link by the trigger pulse. This procedure triggers the spark gap switches, but since the Marx generator capacitor bank has not been charged, no Marx pulse occurs. Using this method, therefore, allows the analysis of the effects of electrical noise generated by the trigger circuitry alone.

To analyze the effects of noise generated by the FXR generator alone, the following procedures can be followed to avoid the use of the trigger circuitry (again, refer to the pulserad operations manual and the thesis of Renee B. Pietruska as required).

1. Connect the data link and instrumentation being used for the IEMP experiment in question.
2. Perform the necessary steps to prepare the FXR generator for normal operation, including pressurization of the spark gap switches to the appropriate level, initialization of the high voltage power supply, and charging of the Marx bank. However, do not arm the trigger generator panel.

3. When the Marx bank reaches the user-determined voltage, reduce the gas pressure in the Marx bank spark gap switches until they discharge. The Marx bank discharge will force the remaining gas switches to fire, resulting in a normal discharge without the use of the trigger generator circuitry.

Note: This procedure has the potential to cause damage to various components in the FXR generator and should only be used when the preceding method yields inconclusive results.

The use of the two procedures listed above should allow the isolation of the offending component, be it in the FXR generator itself, or in the trigger circuitry. In any event, the elimination of electrical noise in the NPS FXR facility can be a difficult task, and researchers should set aside sufficient time in their research proposals for the elimination of noise sources and the establishment of an acceptable data collection system.

## V. PREDICTION OF PHOTON INDUCED ELECTRON YIELDS FOR WAFER SCALE INTEGRATED DEVICES

In order to design appropriate instrumentation to collect useful data on the effects of IEMP on wafer-scale devices, some general predictions of yield need to be developed. Due to the infinite possibilities that exist in SiPCB design layout, it would be impractical to develop exact relationships that would be accurate for all cases. Therefore, in this section, generalized results will be obtained for the expected yield of an incremental conductor element under ideal conditions so that results can be obtained for other configurations by extrapolation.

Figure 5.1 shows the general case to be analyzed. It represents a two micron thick metalized gold film deposited on a silicon substrate and is, in fact, a cross-section of the temperature sensor presented in Figure 2.5. The sample element analyzed here assumes a total irradiated surface area of  $0.05 \text{ cm}^2$ .

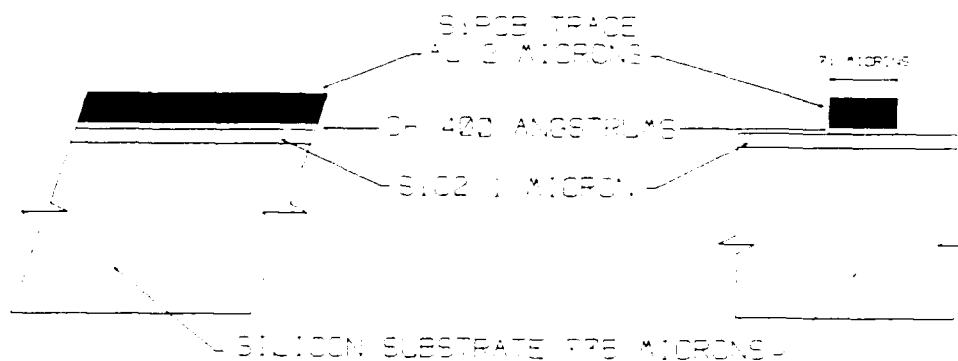


Figure 5.1 Cross section of Two Micron Thick Temperature Sensor (See Figure 2.5)



To determine the maximum expected electron yield for this sample element, the intensity and energy of the incident X-ray beam must be known. The average values of these parameters can be obtained from the Pulserad 112A specification sheet (Table 4.1) and the characterization data collected in the thesis of Renee B. Pietruska [Ref. 10]. However, the values obtained from these sources are of an unrestricted beam. Irradiation of an area of  $0.05 \text{ cm}^2$  requires the use of a shield composed of a high atomic number material (usually lead) with a through hole to limit the irradiation to the target area.

The thickness of the lead chosen here was 1 inch. Experimental data indicates that, for a  $0.05 \text{ cm}^2$  aperture, the through-hole dose will be approximately twice that obtained through the lead, with sufficient dose reaching the target to provide a measurable level of signal.

This 2-to-1 dose ratio is hardly ideal. It would be preferable to have at least a 10-to-1 ratio to insure that only areas of interest are irradiated with significant quantities of X-rays. Unfortunately the generation of the X-ray pulse by the Bremsstrahlung process is far from tidy. Figure 5.2 shows the ideal process, where all Bremsstrahlung photons travel straight, predictable paths. Were this the case, the X-ray attenuation through the 1 inch of lead would be approximately 90% (Table 5.1).

Figure 5.3 depicts the actual scenario, where countless collisions between electrons, Compton scattering, tantalum integrity, and other non-ideal processes produce a non-uniform photon output. This greatly reduces the effectiveness of the aperture/shield arrangement as an X-ray directing technique.

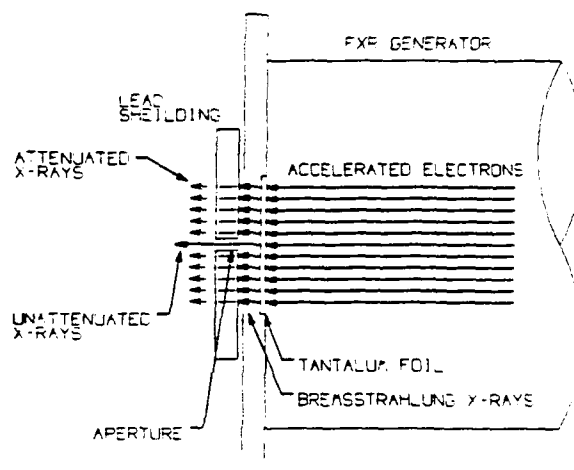


Figure 5.2 The Bremsstrahlung Generator and Shielding Under Ideal Conditions

TABLE 5.1 ATTENUATION CHARACTERISTICS OF LEAD AS MEASURED AT THE NPS FXR FACILITY

Measured Dose Versus Lead Thickness at 100 KV Charge on Marx Bank at Pulserad 112A Face

<u>Lead Thickness in Inches</u>	<u>Dose in ROENTGENS</u>
1/8	18.07
1/4	11.56
3/8	7.74
1/2	5.39
5/8	4.02
3/4	2.95
7/8	1.45
1 inch	1.93

General Relationship (Approximate) between Attenuation and Shield Thickness

$$\alpha = \left[ \frac{1}{2} \right]^N$$

$$T_t = NT$$

$\alpha$  = attenuation desired

T = 1/2 dose thickness

N = number of 1/2 dose thicknesses required

$T_t$  = total shield thickness

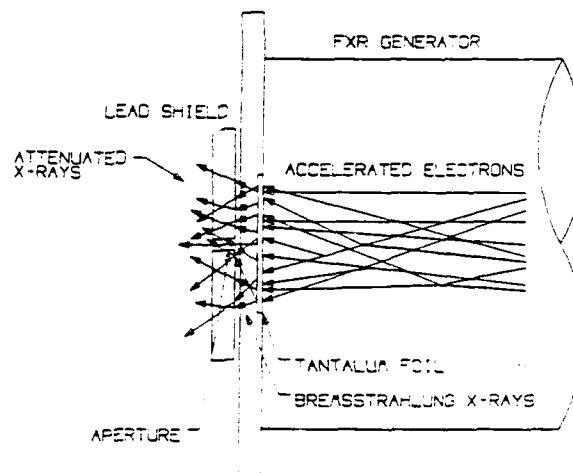


Figure 5.3 The Bremsstrahlung Generator and Shielding under Actual Conditions

Using this lead shield and aperture, the dose expected at the target will be greatly reduced. As an example, the exposure derived from Table 5.2 and Figure 5.4 for a distance of 3.6 cm from the anode face (a minimum distance determined by hardware constraints) is 916 Roentgens (R). Experimental data obtained using a one inch thick lead shield with a 0.05 cm<sup>2</sup> aperture and 3.6 cm total distance to the dosimeter is approximately 5 R. The large disparity between the two results illustrates the value of experimentally-obtained dose information. Since the dose delivered through a complex shielding geometry is very difficult to predict, all dose information presented here will be experimentally derived.

Using the approximate value of 5 R obtained above, an average photon energy of 0.7 MeV (derived by taking the average value of the pulse in Figure 4.2b, approximately (1.7 MeV)(.4)  $\cong$  0.7 MeV) and Table 5.3, the X-ray beam intensity can be estimated.

TABLE 5.2 ON-AXIS MEASURED EXPOSURE AT VARIOUS  
DISTANCES FROM THE ANODE FACEPLATE (100 kV)  
[Ref. 10:p. 115]

Distance (cm)	Exposure (R)
0.64	2290
1.27	2180
1.90	1309
2.54	1064
5.08	693
10.16	255
15.24	125

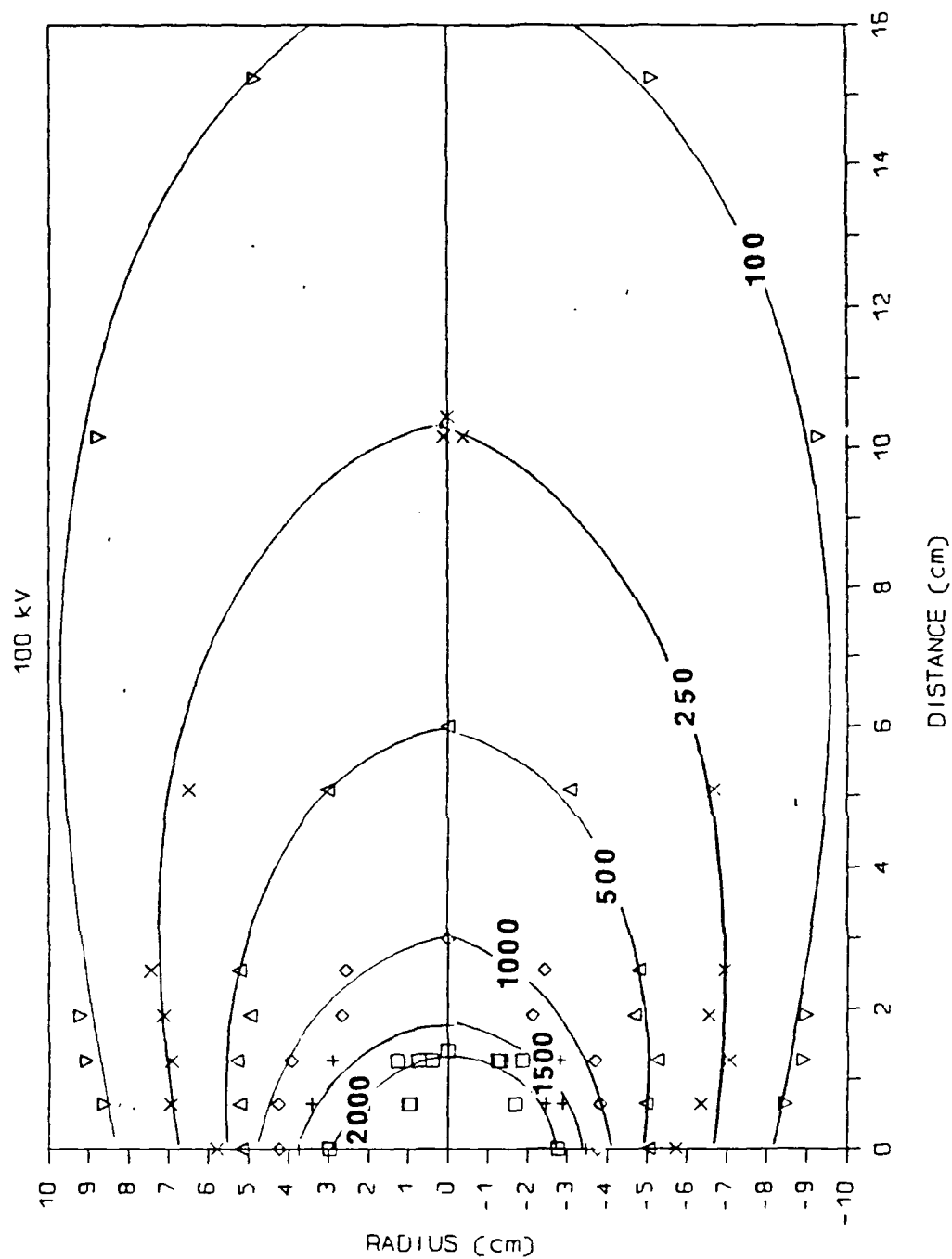


Figure 5.4 Pulserad 112A 100 kV Contours of Constant Exposure (R), as Measured with  $\text{CaF}_2\text{:Mn}$  TLD's. [Ref. 10:p. 117]

TABLE 5.3 PHOTON FLUENCE PER RAD(Si) AS A FUNCTION  
OF PHOTON ENERGY [Ref. 5:pp. 3-28]

Energy (MeV)	Intensity ( $10^8$ photons/cm <sup>2</sup> )
0.1	143.0
0.15	136.0
0.2	108.0
0.3	71.0
0.4	53.0
0.5	42.0
0.6	35.0
0.8	27.0
1.0	22.4
1.5	16.2
2.0	12.9
3.0	9.4
4.0	7.4
5.0	6.1
6.0	5.2
8.0	4.0
10.0	3.2

The estimated value is:

$$(31 \times 10^8 \text{ Photons/cm}^2 \text{ Rad(Si)})(5 \text{ R}) \cong 1.6 \times 10^{10} \text{ Photons/cm}^2 \quad (5.1)$$

where

1 radiation absorbed dose in silicon ( $\text{Rad(Si)}$ )  $\approx 1 \text{ R}^*$

To determine the actual photon yield, the following relationship can be used [Ref 5:pp. 4-4,4-5]:

$$\Phi_p = \int \frac{1}{r^2} P_t \cos \lambda \frac{dPe}{d\Omega'} dV dE \text{ Photoelectrons/cm}^2 \quad (5.2)$$

where

$\Phi_p$  = photoelectron fluence,

$P_t$  = electron escape probability,

$\lambda$  = electron scattering angle,

$1/r^2$  = fluence dispersion factor in the solid angle,

$dPe/d\Omega'$  = differential volume source of photoelectrons per unit solid angle,

$V$  = volume of target, and

$E$  = energy of photons.

When the individual terms above are expanded, the expression for  $\Phi_p$  becomes quite imposing, and for several of the terms only an approximate closed form is possible. Fortunately, graphical techniques are available and are in standard use to avoid the problems of obtaining a numerical solution for  $\Phi_p$ .

---

\* 1 Rad deposits  $10^{-2} \text{ J/kg}$  of energy in a material (silicon in this case), while 1R deposits  $8.7 \times 10^{-3} \text{ J/kg}$ . These values are similar enough to be considered equal for the approximations applied here. [Ref. 14:p. 1021]

For the photon energy levels of interest here, and for a gold target (Atomic number = 79), the Compton effect dominates over the photoelectric effect and pair production as can be seen in Figure 5.5. The photoelectric fluence ( $\Phi_p$ ) can be approximated by the use of Figure 5.6a, which is a set of composite curves combining the Compton ( $\phi_e$ ) and photoelectric fluence effects (Figure 5.6b). In Figure 5.6, it is assumed that  $P_t$  is sufficiently small to justify the omission of the sample element thickness as a pertinent parameter (since for  $P_t \ll 1$ , thin and thick targets will have a similar yield).

From Figure 5.6a, the sample element is seen to have a photoelectric fluence of  $7 \times 10^{-3}$  electrons/photon for an average photon energy of 0.7 MeV. Using the value of intensity previously obtained ( $1.6 \times 10^{10}$  photons/cm<sup>2</sup>), it can be seen that  $1.1 \times 10^8$  electrons have been displaced from the sample element by the incident photons. This leaves a positive charge of  $1.8 \times 10^{-11}$  Coulombs. Assuming a FXR output pulse width of 20 nanoseconds (Table 4.1), a current of approximately 900 microamperes is expected to occur between the earth ground and the sample element, assuming a charge equalization time similar to the FXR pulsewidth.

This yield prediction is, to say the least, highly speculative. Results depend not only on the Compton yield of the target, but also upon the effects of surrounding media (including the insulating substrate of Figure 5.1) and other effects not addressed here. Furthermore, the actual X-ray yield of the FXR generator varies dramatically from day to day, depending on the conditions of its various component parts and random factors associated with each individual shot. Variations of several hundred percent from this projected yield can be expected, and the 900 microamp prediction should be considered a mean value, useful primarily as



an aid in the design of the data collection apparatus. Some of these variations can be minimized by ensuring the use of a relatively clean cathode and anode for a

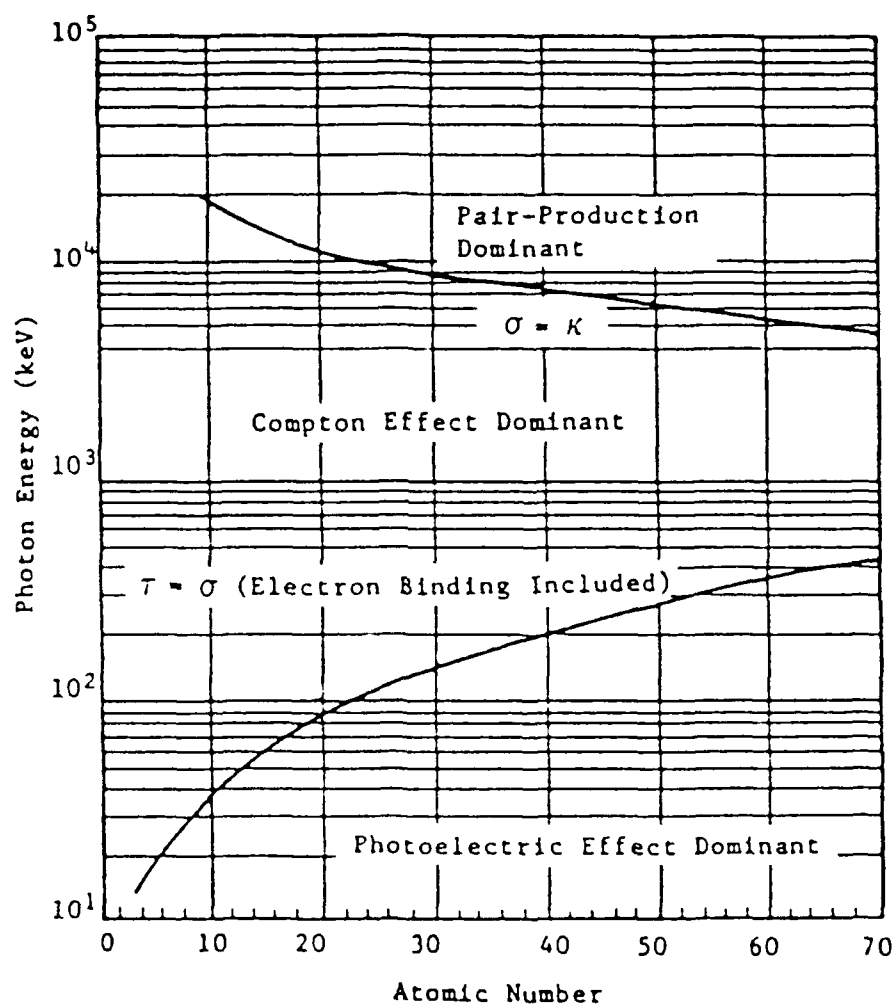


Figure 5.5 Relative Importance of the Photoelectric and Compton Effects, and Pair-Production as a Function of Atomic Number and Photon Energy [Ref. 5:pp. 3-24]

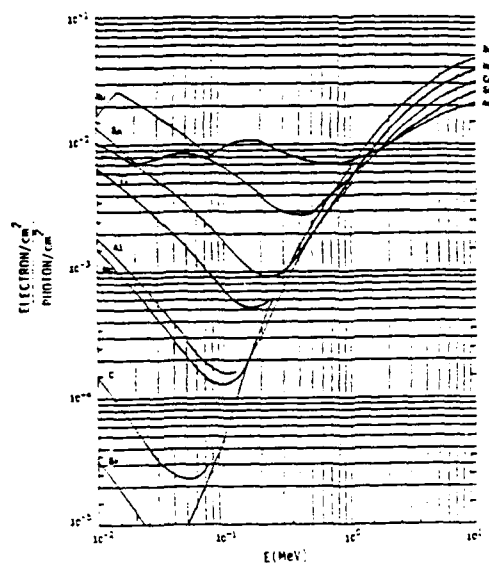


Figure 5.6a Maximum Photoelectric and Compton Electron Emission (Current) Per Photon for Normally Incident Monoenergetic Photons [Ref. 5:p. 4-5]

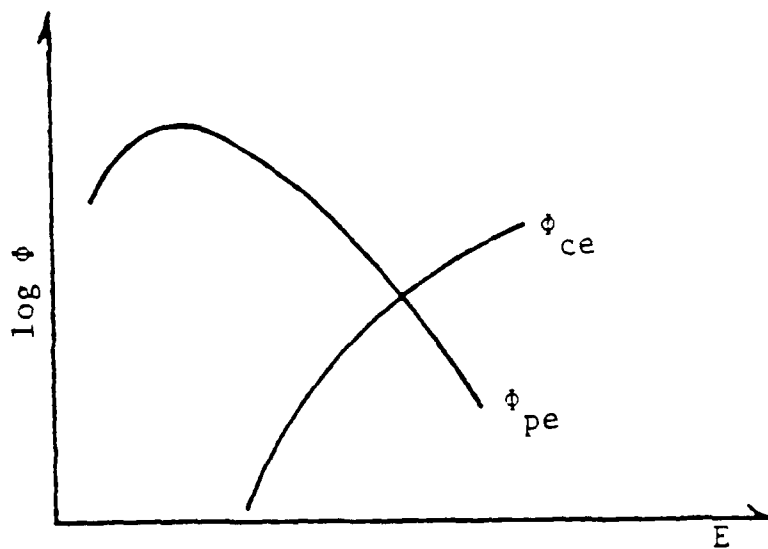


Figure 5.6b General Photon Energy Dependence of  $\Phi_c$  and  $\Phi_p$  [Ref. 5:p. 4-3]

particular experiment. Note that, for the energy levels of interest here, most metals will have a similar yield and may be used interchangeably for convenience (Figure 5.6a).

The method of measuring this photoelectric current is illustrated in Figure 5.7. This simple arrangement allows the fast current pulse to be measured indirectly, by detecting the voltage drop across a load resistor and applying Ohm's law. The value chosen for this resistor was  $100\ \Omega$  (the reasons for this choice will be made clear in Section VI). Using the 100 ohm load resistor, the expected signal level will be 90 millivolts.

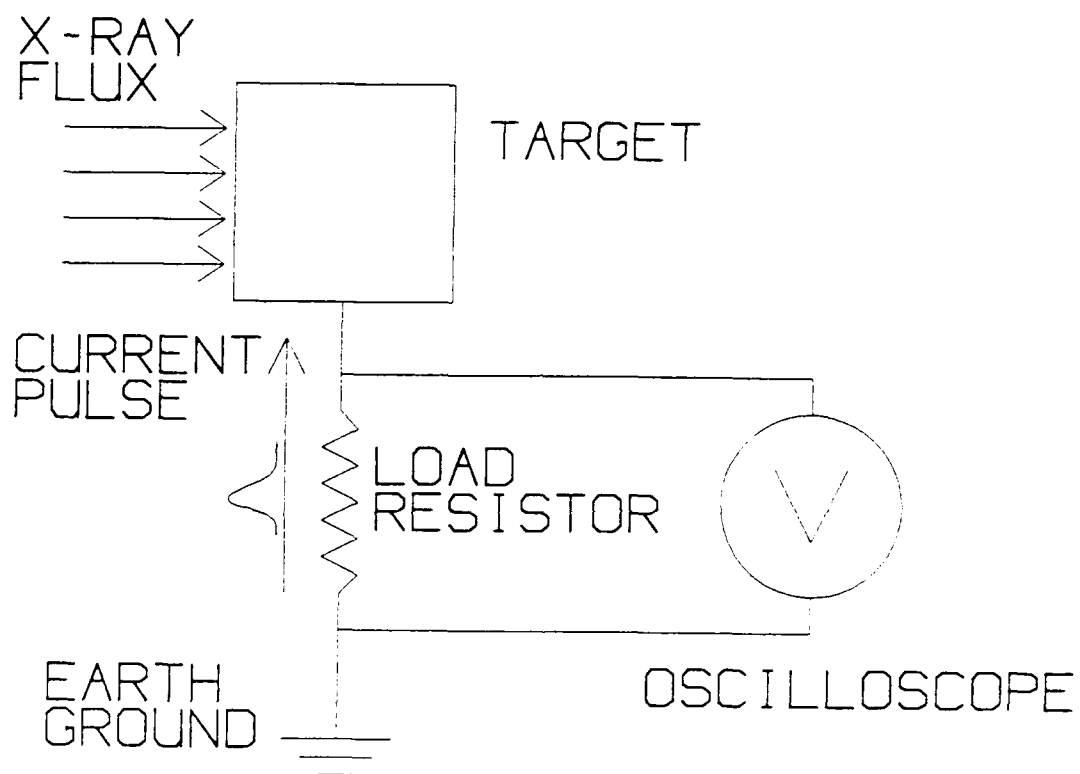


Figure 5.7 Indirect Measurement of the Photon Induced Current Pulse

## VI. INSTRUMENTATION REQUIREMENTS FOR THE MEASUREMENT OF IEMP IN WAFER-SCALE INTEGRATED DEVICES AT THE NPS FXR FACILITY

The noise problems discussed in Section IV and the modest yields predicted in Section V indicate the need for a data collection system that can provide a high signal-to-noise ratio (SNR) and still provide reasonable fidelity over a wide bandwidth in a high noise environment. Preliminary tests have shown that simple unbalanced coax or triax data links are inadequate for the task, regardless of how the shields are connected, due to their low immunity to electrical noise. This section provides sufficient information to allow researchers to construct, test and troubleshoot suitable data collection apparatus for use in the NPS FXR facility.

Since the majority of frequency components contained in the EMP are below 20 MHz (with a wavelength longer than 15 meters), most electrical noise pickup occurs in the data link from the radiation exposure area to the instruments in the RFI enclosure, a data cable distance of approximately 20 meters.

To reduce the effects of the radiated EMP on data collection links, several special techniques may be applied. Two of the most promising techniques have been investigated here, and their advantages and shortcomings will be described.

To increase noise immunity, the data link from the radiation area to the instrumentation may be a fiber optic link rather than conventional electrical coaxial cables. The expression relating the time average power induced in a linear conductor by an external electromagnetic field is [Ref. 15:p. 485]

$$P_{av} = \eta \frac{\pi}{3} \left[ \frac{I_0 d}{\lambda} \right] \quad (6.1)$$

where

$\eta$  = impedance of free space =  $120 \pi$  ohms,

$I_o$  = current induced in conductor in amperes,

$d$  = conductor length in meters,

$\lambda$  = wavelength of induced current in meters, and

$P_{av}$  = time average power induced in conductor in watts.

It can be seen that in order to reduce the level of power induced in a conductor, it must be very short in comparison to the wavelength and, for conductor lengths of less than one quarter wavelength, the coupling efficiency becomes quite small and little power is induced in the conductor.

The use of a fiber optic cable in lieu of an electrically conducting one reduces the  $d$  term in Eq. 6.1 to zero, thus completely eliminating electrical noise pickup in the data link itself. This leaves only the data collection instrumentation attached to the fiber optic cable as a potential source of unwanted electromagnetic interference pickup.

To protect the target and data collection instrumentation from the above noise, the entire target and associated instruments should be enclosed in a Faraday cage or other shielded enclosure. Figure 6.1 is a cutaway diagram of the Faraday cage built for this investigation showing the arrangement of the target and associated data collection and transmission modules.

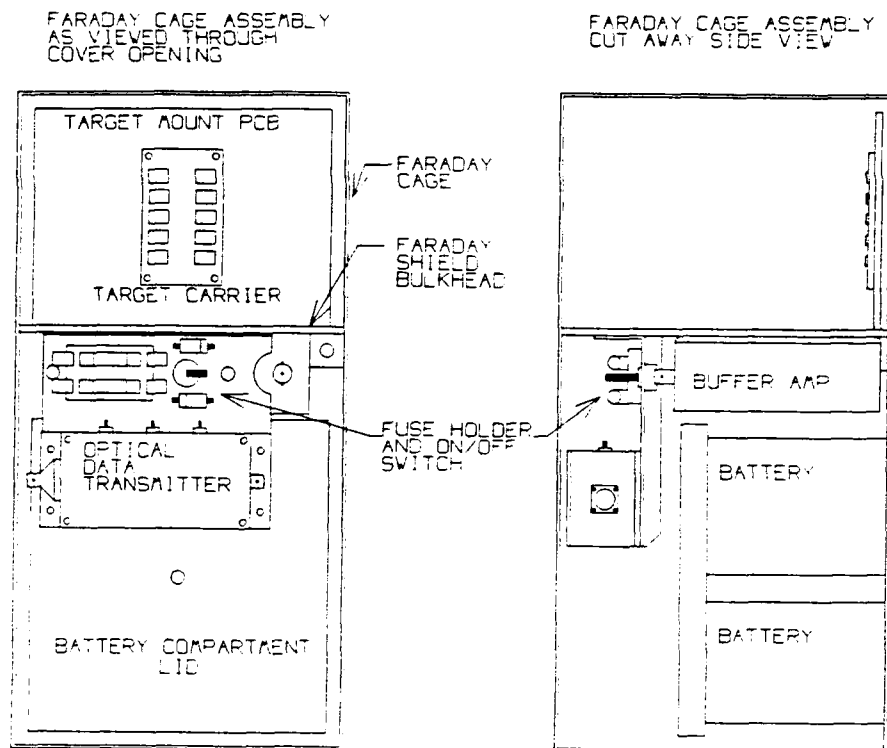


Figure 6.1 Cutaway Diagram of Faraday Cage Showing Arrangement of Target and Data Collection and Transmission Modules

Generally a Faraday shield should be constructed of mu metal for maximum attenuation of the electromagnetic interference. Considering the relationship for conduction current density and electric field intensity with penetration into a conductor [Ref. 15:p. 400],

$$\delta = \frac{1}{\sqrt{\pi f \mu_0 \mu_m \sigma}} \quad (6.2)$$

where

$f$  = frequency of electromagnetic wave in Hertz,

$\mu_0$  = permeability of free space =  $4\pi \times 10^{-7}$  H/m,

$\mu_m$  = permeability of conductor (dimensionless),

$\sigma$  = conductivity of conductor in mhos per meter  $(\Omega m)^{-1}$ , and

$\delta$  = depth of penetration (skin depth) in meters

= depth where power density is reduced to  $e^{-2}$  of incident value.

It can be seen that for a given frequency, the depth of penetration of an impinging electromagnetic wave is *inversely proportional to the square root of the permeability and conductivity of the shielding material*. Table 6.2 is a list of normalized skin depths for various materials suitable for fabricating electronic enclosures. It can be seen that magnetic materials are significantly better than non-magnetic materials at lower frequencies for shielding purposes due to the large permeability of the former. ("Better" implies a smaller skin depth).

In addition to having the electronics enclosed in the Faraday cage, the power source for the data collection instruments (the batteries in Figure 6.1) should also be enclosed. This eliminates the possibility of external power supply conductors introducing EMP into the Faraday cage and subsequent enclosed circuitry. The *only penetration of the shielded Faraday assembly should be for the optical cable, an unavoidable necessity*.



**TABLE 6.2 CONDUCTIVITY, PERMEABILITY AND NORMALIZED SKIN DEPTH  
FOR COMMON SHIELDING MATERIALS. TO FIND ACTUAL SKIN DEPTH,  
DIVIDE NORMALIZED VALUE BY THE SQUARE ROOT OF THE  
FREQUENCY OF INTEREST**

$$(\delta = \delta_n / \sqrt{f}) \text{ [Ref. 8:p. 132]}$$

<b>Material</b>	<b>Conductivity (<math>\Omega\text{m}</math>)<sup>-1</sup></b>	<b>Permeability (H/m)</b>	<b>Normalized Skin Depth <math>\delta_n</math> (Centimeters/(sec)<sup>-1/2</sup>)</b>
Aluminum	3.5x10 <sup>7</sup>	1	8.50
Copper	5.8x10 <sup>7</sup>	1	6.1
Brass	1.6x10 <sup>7</sup>	1	12.6
Tin	8.7x10 <sup>6</sup>	1	17.1
Zinc	1.9x10 <sup>7</sup>	1	11.5
Lead	4.5x10 <sup>6</sup>	1	23.7
Nickel	1.3x10 <sup>7</sup>	50	1.97
Iron (pure)	1.0x10 <sup>7</sup>	4x10 <sup>3</sup>	0.252
mu metal(typical)	1.6x10 <sup>7</sup>	2.0x10 <sup>4</sup>	0.089

Another important aspect of shielding is the problem associated with ground loops. A ground loop occurs when the grounding point of several components or instruments occurs at more than one location. This in effect creates a loop antenna that may be quite efficient at picking up radio frequency interference occurring at certain frequencies and attitudes as well as causing dc currents that may cause offset errors, both of which couple into the signal path. Figure 6.2 shows two hypothetical instrumentation set-ups, one showing obvious ground loops and the other deliberately configured to avoid these loops. Since the actual grounding configurations for various items in the FXR environment are uncertain, some

experimentation may be warranted in an effort to reduce noise pickup by instruments and re-radiation from seemingly innocent items (such as electrical conduits or shielded cables).

When each instrument block by itself is shielded and a Faraday cage is being utilized, then each block should be securely grounded to the Faraday cage interior surface, with minimum length signal cables used.

The block diagram of the entire fiber optic data link is shown in Figure 6.3 and the experimental setup is illustrated in Figure 6.4.

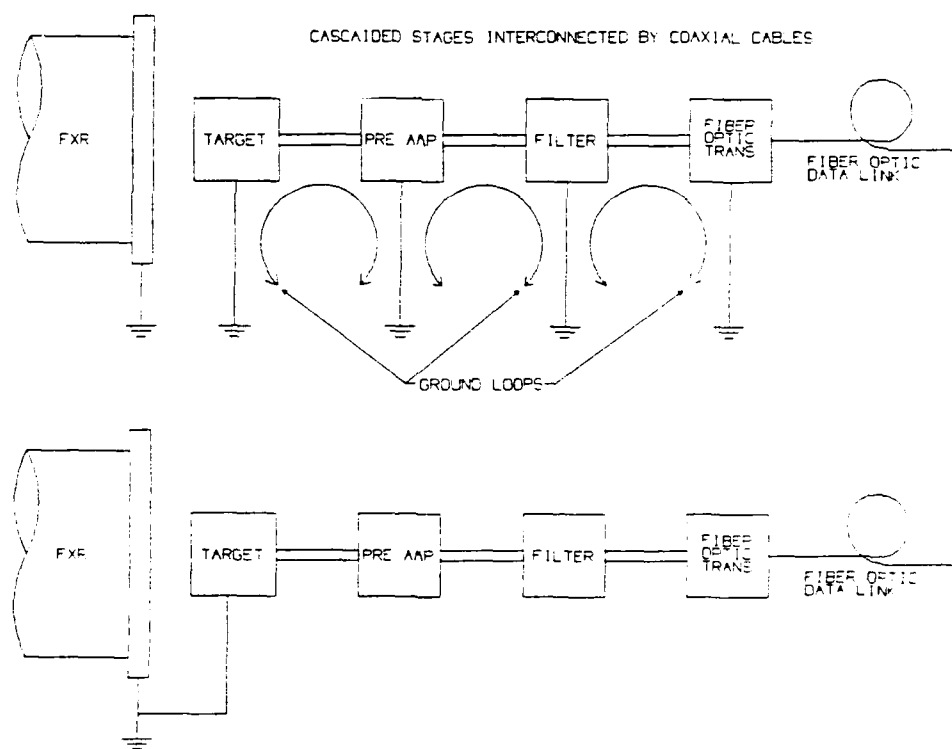


Figure 6.2 Hypothetical Instrumentation Showing Ground Loops (TOP) and a Reconfigured Version with Ground Loops Eliminated (BOTTOM)

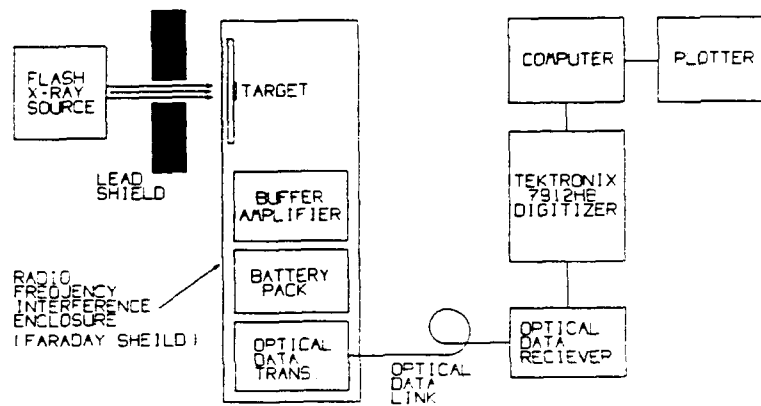


Figure 6.3 Block Diagram of Fiber Optic Data Link

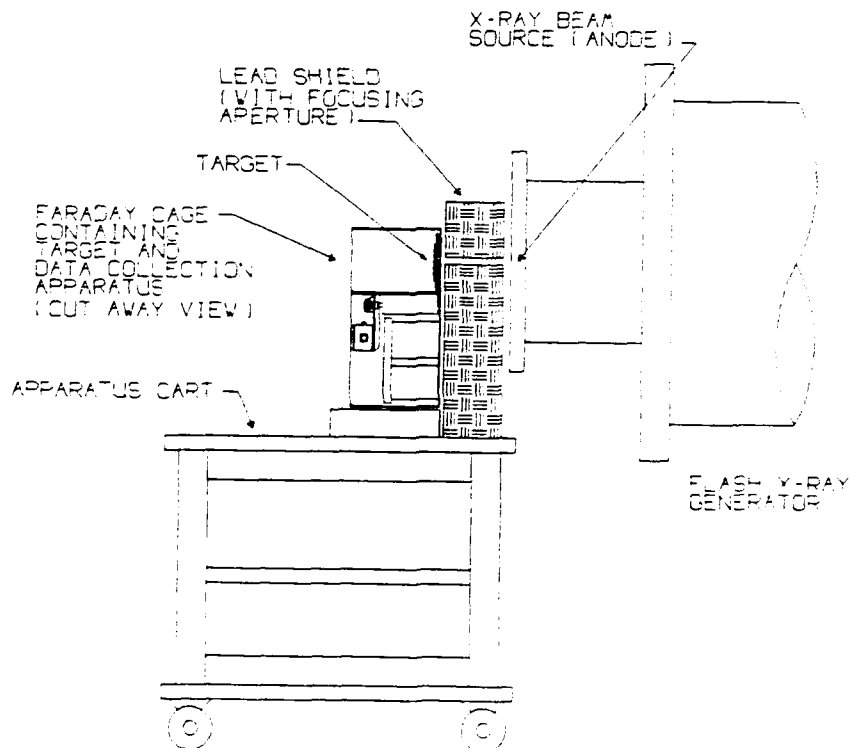


Figure 6.4 Experimental Setup for Fiber Optic Data Link

The second method investigated for data collection in the NPS FXR facility consists of a differential data link. The differential cable concept is illustrated in Figure 6.5. Note that the desired signal is applied differentially to the parallel conductor pair and thus can be recovered at the receiver end with a differential amplifier, while electrical noise is applied to the parallel conductors equally (common mode) and is rejected by the differential amplifier (Figure 6.6). The block diagram for the differential data link is shown in Figure 6.7. Note that the shielding techniques previously referred to must be observed to protect the contents of the target shielding box.

#### **A. LIMITATIONS OF FIBER OPTIC AND DIFFERENTIAL DATA LINKS**

The two methods of data collection in the NPS FXR facility discussed above have proven to be the only suitable techniques available for adequate data fidelity. However, these methods each have limitations that limit their usefulness.

In the case of the fiber optic link, the limiting factors are electrical noise pickup in the Faraday target box, and noise generation in the optical receiver (photo avalanche detector or pin diode). The former problem arises in part by nature of the complexity of the circuitry required in the target box. The numerous electronic components necessary to perform the buffering, amplification and optical modulation have a tendency to be adversely affected by EMP as well as IEMP. This problem can be solved only by the use of a carefully designed Faraday enclosure to limit EMP, and the use of thick lead shielding to protect the electronics from photon effects. The thickness of the lead shielding may have the additional

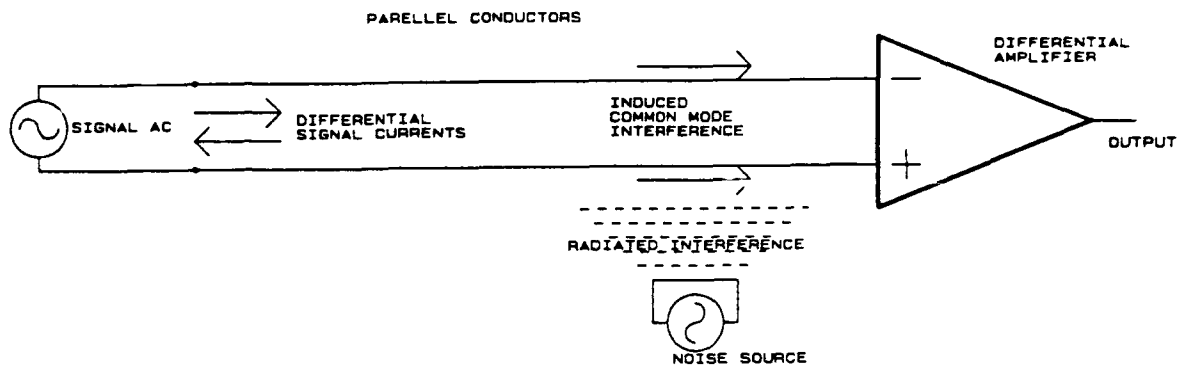


Figure 6.5 Schematic Representation of a Differential Data Link

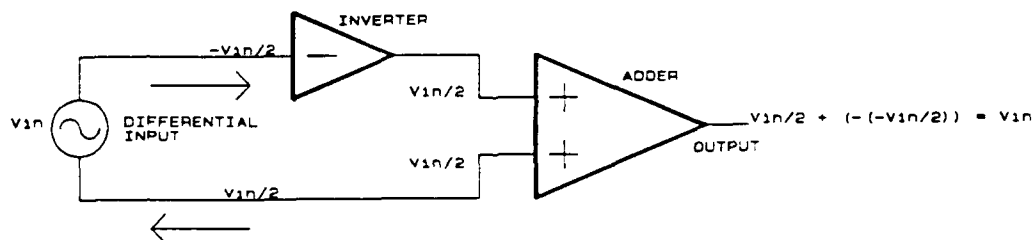
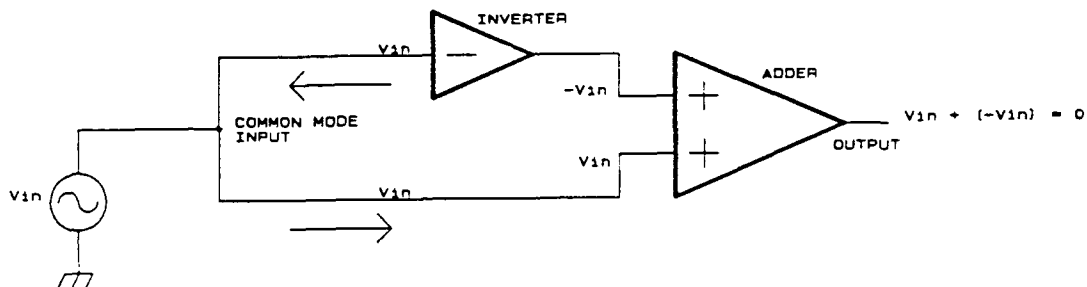


Figure 6.6 Differential Amplifier Equivalent Circuit and its Response to Common-mode and Differential-mode Signals

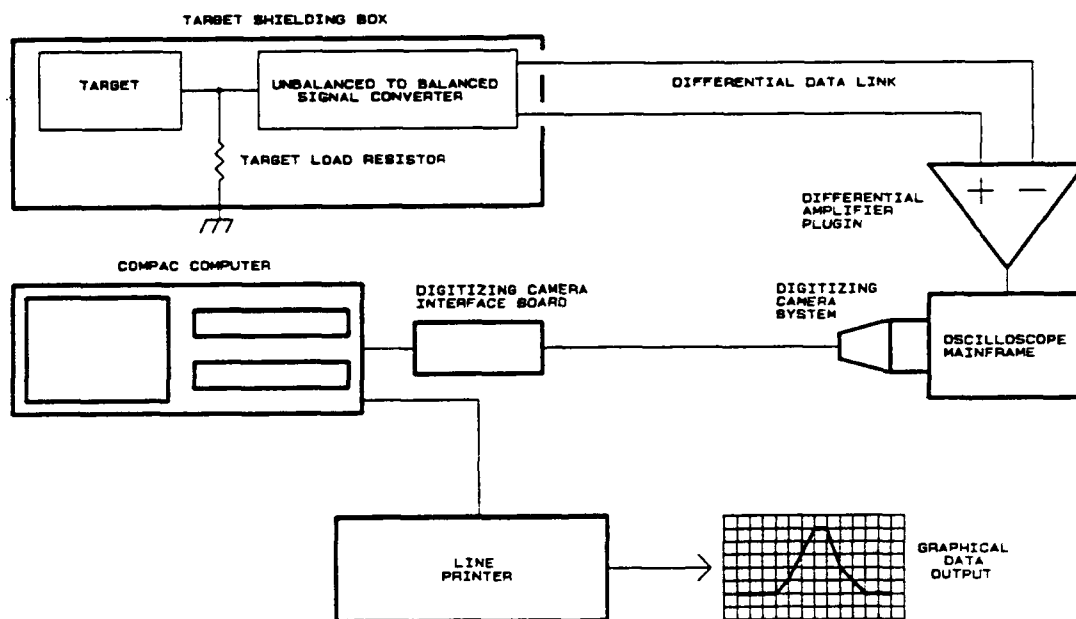


Figure 6.7 Block Diagram of the Differential Data Link and Instrumentation

detrimental effect of reducing the photon dose at the target which subsequently reduces the electron yield, lowering the SNR even further.

The mean square-noise power generated in the optical receiver can severely limit the signal-to-noise ratio of the system by introducing a background noise level approaching that of the expected signal. Experimental results indicate that for a Merit Inc. Model R26911TV-GD Photoavalanche optical detector module, the expected noise level will be 15–20 mV<sub>pp</sub> across a 50  $\Omega$  load (the preferred units for expressing photon-induced data is volts). The use of a PIN diode in lieu of a photoavalanche detector reduces this noise level by an order of magnitude or greater. Additional problems with fiber optic systems include the high cost of components and the difficulty in the field installation of fiber optic connectors onto cables. A major bonus that fiber optic systems possess is the large bandwidths attainable (up to 120 MHz for light emitting diode transmitters and many gigahertz for laser-based systems).

For a differential data link, the primary problems encountered are limited bandwidth and difficulty in obtaining a sufficiently high common-mode rejection ratio to provide adequate data fidelity. The problem of EMP and IEMP pickup in the target box is greatly reduced by nature of the small physical size of the target enclosure and the ability to construct the data acquisition and cable driver circuits using only passive components.

After considerable experimentation and design iterations, the differential data link was selected as being the most versatile, low noise and cost effective method of data collection in the NPS FXR facility and no further work on fiber optic links was pursued. The following section will describe in detail the differential

instrumentation setup established for the irradiation of wafer-scale integrated devices and other small scale electronics components.

#### **B. THE DIFFERENTIAL DATA COLLECTION METHOD AS APPLIED TO THE NPS FXR FACILITY**

A specific variation of the differential data collection method has been applied at the NPS FXR facility. This application has proven to be the most suitable technique tried for collection of data from the photon irradiation of wafer scale integrated devices.

Figure 6.8 shows the cable configuration used for the differential data link. It consists of two Amphenol 21-204 50 $\Omega$  triax cables carefully twisted together with 13 twists per meter. The assembly is wrapped with plastic electrical tape to prevent unraveling. The purpose of twisting the cables together is to insure that any electrical noise applied to the dual cable assembly induces equal noise currents on each cable. This common mode signal can then be canceled out as was described in Figure 6.6.

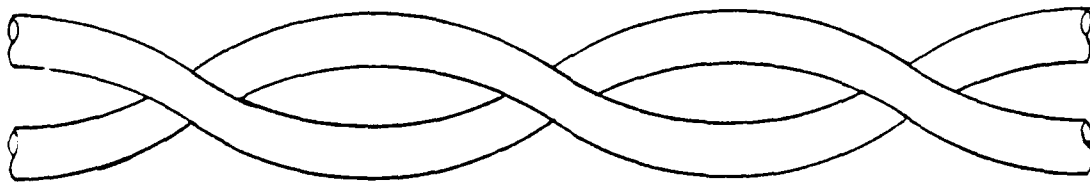


Figure 6.8 Twisted Pair Triax Differential Cable Assembly

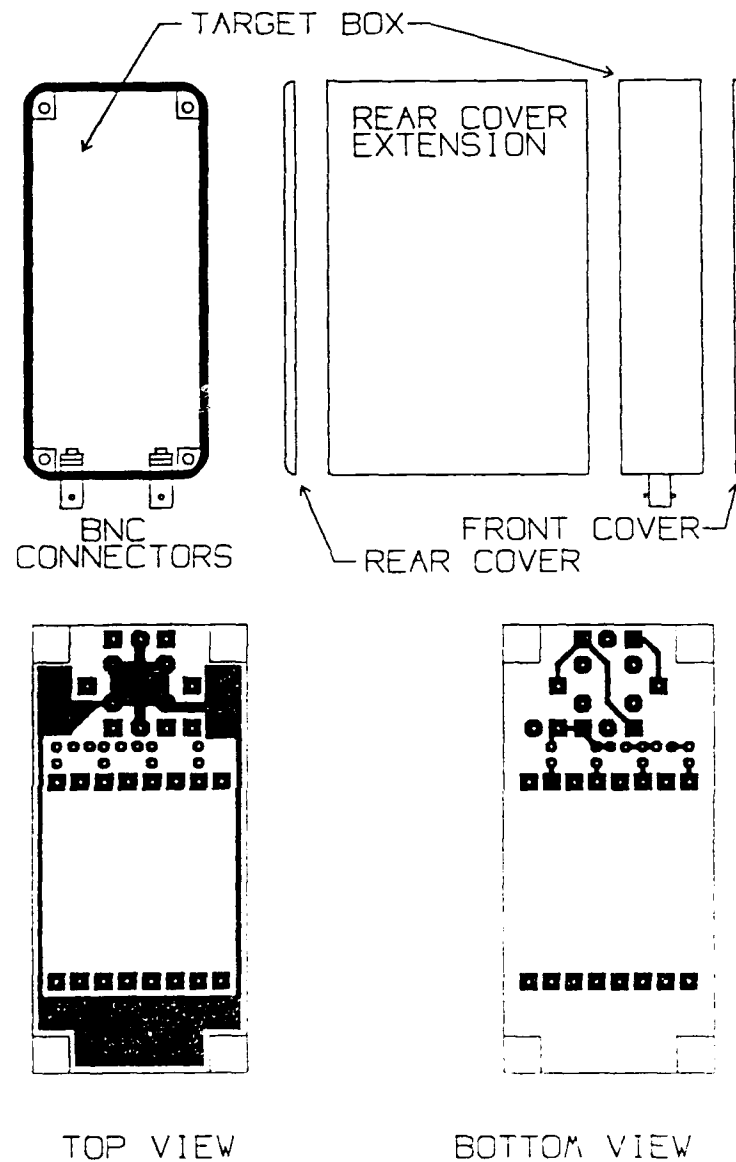


The cable ends are provided with BNC connectors to be compatible with most common test equipment. The two separate shields on each of the triax cables are shorted together at the BNC connectors and are treated as one shield at this point, since this has proven to be the interconnecting method providing the highest noise immunity. The overall data link is approximately 20 meters long and is installed in the cable rack connecting the radiation area with the instrumentation located in the RFI enclosure (see Figure 4.4).

The wafer-scale device to be radiated is fitted into a compact cast-aluminum box (the data collection system being described provides sufficient noise immunity without the need for a mu metal enclosure). This target box configuration, as well as the printed circuit board designed for mating to the wafer-scale device, is shown in Figure 6.9. The printed circuit board provides a plug-in mounting for the wafer-scale sample as well as appropriate interconnects for the other components needed to drive the data link previously described. The wafer-scale carrier is displayed in Figure 6.10.

Figure 6.11 shows a schematic diagram of the target box connected to the data link. The target load resistor will have a voltage induced across it when the wafer scale device is irradiated with photons as a result of the Compton effect (see Figure 3.6, 5.7). This load resistor must be  $100\ \Omega$  to provide a proper impedance match to the data link as will be demonstrated shortly.

The transition from an unbalanced to a balanced load, as well as appropriate impedance matching, is accomplished by the use of a balun (balanced to unbalanced) transformer. The use of active electronic circuitry has proven to be excessively sensitive to noise pickup to be useful for this purpose.



PRINTED CIRCUIT BOARD FOR USE  
WITH WAFER SCALE DEVICE

Figure 6.9 Target Box Configuration and Printed Circuit Board Designed for  
Use with Wafer Scale Temperature Sensor of Figure 2.5

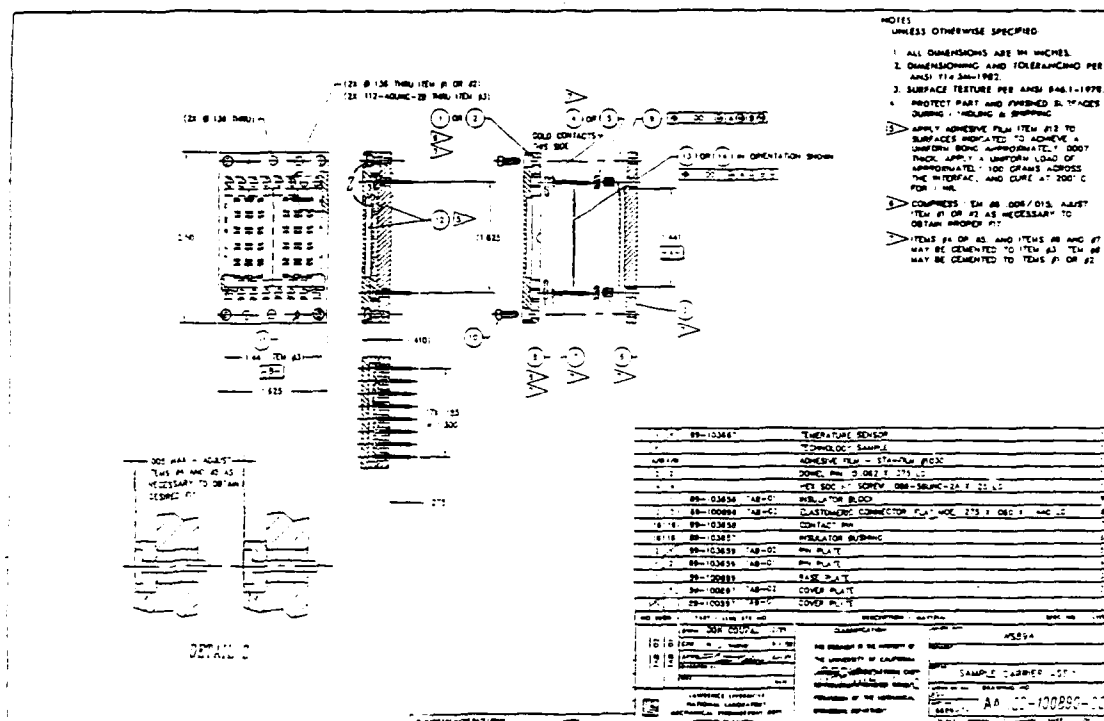


Figure 6.10 Sample Carrier Assembly (Courtesy of Joe Kimbrough, LLNL)

Figure 6.12 illustrates the concept of the balanced transformer when used to drive two coaxial cables. Figure 6.12a shows the arrangement for constructing a 1-to-1 balun transformer. Note that the primary resistor has one end to ground while the secondary resistor has a phantom ground occurring at its center, thus it is balanced with respect to ground. If the secondary resistor is split in two, their junction can be grounded without altering the circuit as shown in Figure 6.12b. Finally it can be seen in Figure 6.12c that properly terminated coaxial cables can be installed in lieu of each of the secondary resistors. If the cable impedance is  $50\ \Omega$  (as in the case of the Amphenol 21-204 triax cable used in the twisted pair differential data link), the primary resistance must be  $100\ \Omega$  to maintain proper impedance matching.

There are numerous other balun configurations that may prove useful to researchers, primarily to allow the use of a target resistance greater than  $100\ \Omega$ . Figure 6.13 illustrates two of these baluns with impedance transformation properties. Note that as the impedance transformation ratio becomes larger, the transformer structure becomes more complex, and bandwidth limitations may result. Furthermore, load resistor values greater than 100 ohms tend to suffer the effects of parasitic capacitances that are inevitable in the circuitry, reducing the bandwidth even further.

For the yields anticipated from photon irradiation of wafer scale devices, the simple 1-to-1 balun has proven to be satisfactory. The physical construction of a suitable wide bandwidth balun transformer is illustrated in Figure 6.14. Here a specialized balun core is used in conjunction with tri-filar wound coils to produce a transformer with a -3dB bandwidth extending from 1.2 kHz to 30 MHz. The use of tri-filar construction insures that each of the three separate windings used in

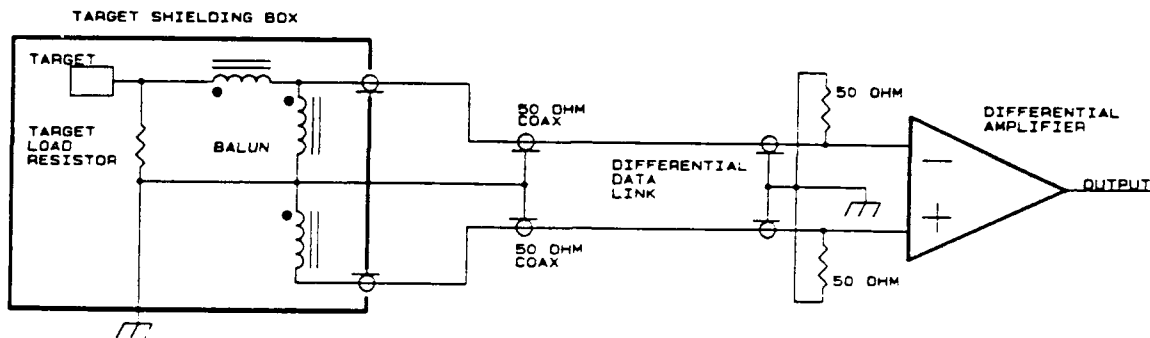


Figure 6.11 Schematic Diagram of the Target Box, Differential Cable Assembly and the Differential Amplifier

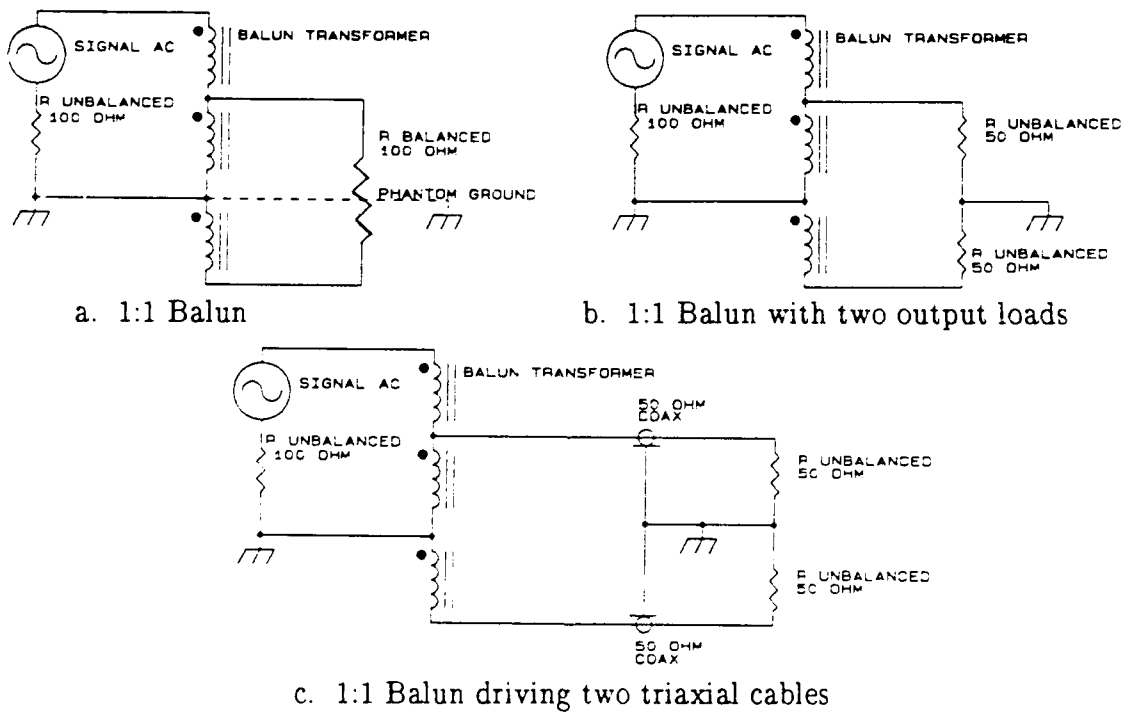


Figure 6.12 a,b,c Concept of the Balun Transformer for Mating between Balanced and Unbalanced Lines

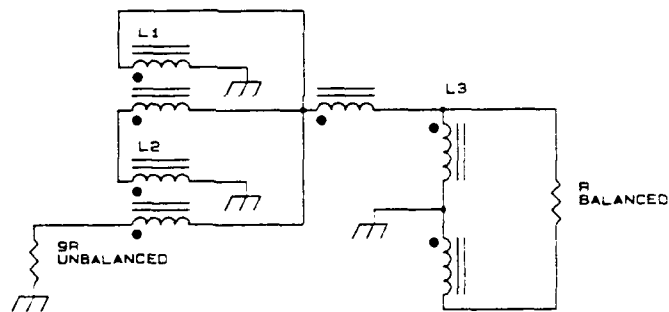
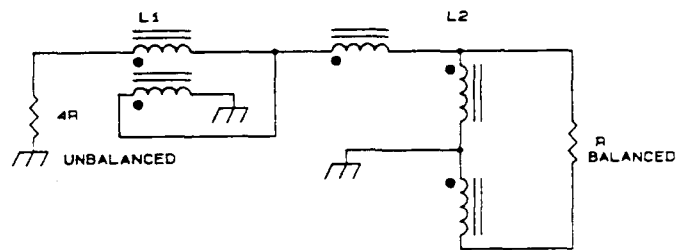
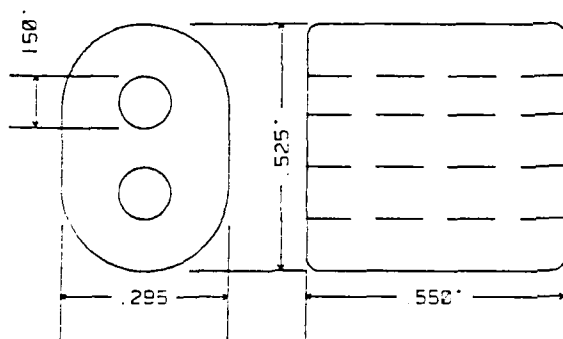
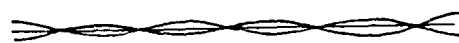


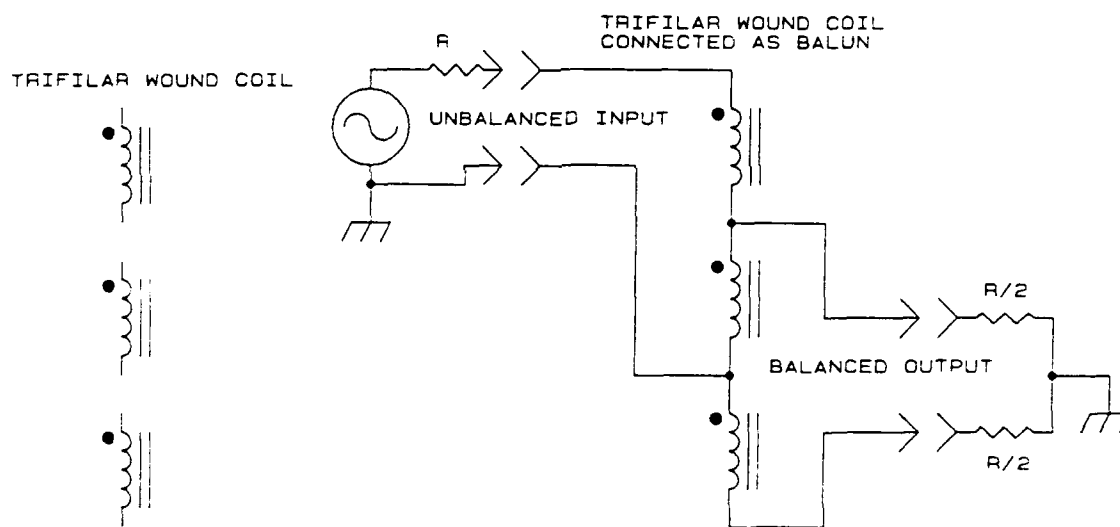
Figure 6.13 Examples of Balun Transformers with Impedance Transformation Properties. The top circuit provides a 4-to-1 impedance transformation, while the bottom circuit provides a 9-to-1 impedance transformation.



a. Ferrite Balun Core



b. Trifilar Wrapped Conductors



c. Trifilar Wound Coil on Ferrite Balun Core

Figure 6.14 a,b,c Construction of a Wideband Balun Transformer

the balun are of the same length, insuring that the differential cable assembly is driven in a balanced, symmetrical fashion. A disadvantage of tri-filar and bi-filar windings is the introduction of additional interwinding capacitance that may cause transformer ringing or limit the upper frequency bandwidth. [Ref. 16:pp. 268-271]

At the receiver end of the differential link a differential amplifier is required. This amplifier can be either a true differential type, or it can be implemented by the use of a dual channel amplifier that is capable of performing the inversion and addition functions depicted in Figure 6.6. However, the use of a dual channel amplifier results in a poor common-mode rejection ratio (CMRR), defined as the differential-mode gain divided by the common-mode gain. This is due to the lack of symmetry in the circuit and the subtle phase and amplitude differences occurring in the two channels. The CMRR resulting from the use of a dual channel amplifier is typically 150 at dc dropping to below 10 at 20 MHz. The ideal value of the CMRR would approach infinity.

True differential amplifiers are the preferred choice when implementing a differential data link. The only notable limitation with the use of a differential amplifier is in the bandwidth. The typical commercially available differential amplifier has an upper -3dB bandwidth of 1 MHz. This limitation is imposed by the manufacturer primarily due to the deterioration of the CMRR as the frequency is increased. The CMRR of most commercial differential amplifier assemblies is 100000 at dc, and typically degrades to 2000 at 1 MHz. This degradation is due to phase and amplitude variations in the amplifier stages, as was the case for dual channel amplification. The limitation is imposed so that a minimum specified CMRR can be guaranteed over the bandwidth of the amplifier.



The amplifier chosen for use with this data link is a Tektronix Model 7A13 differential comparator. This unit can be used as a differential comparator or a differential amplifier, depending on user-selected switch settings. This amplifier is a plug-in device and is used in conjunction with a Tektronix Model 7104 Oscilloscope. The bandwidth of the amplifier is 105 MHz when used in conjunction with the Tektronix Model 7104 oscilloscope and has a CMRR ranging from 20000 at dc, to 200 at 20 MHz (Figure 6.15). The limited CMRR at high frequencies is to be expected and will not adversely affect the noise immunity since experimental data suggests an induced noise level of 1 V<sub>pp</sub> on a triax cable 20 meters in length. A CMRR of 200 will reduce this to approximately 5 mV<sub>pp</sub>, a level far less than the 90 mV<sub>pp</sub> expected signal level.

The analog portion of the data link can now be analyzed in its entirety. Figure 6.16 shows the frequency response of the assembled system, with Figure 6.16a showing the swept response from 200 Hz to 4.4 kHz, and Figure 6.16b showing the response from 200 kHz to 20 MHz. The frequency range of 4.4 kHz to 200 kHz (not shown) possesses a monotonically smooth response.

The CMRR can be determined by the application of an equal signal (Common Mode) to each cable in the differential data link and dividing this signal value by that obtained from the output of the differential amplifier (that value displayed on the 7104 oscilloscope). This yields the CMRR assuming the differential mode gain equals unity in the data link. (A reasonably good assumption.)

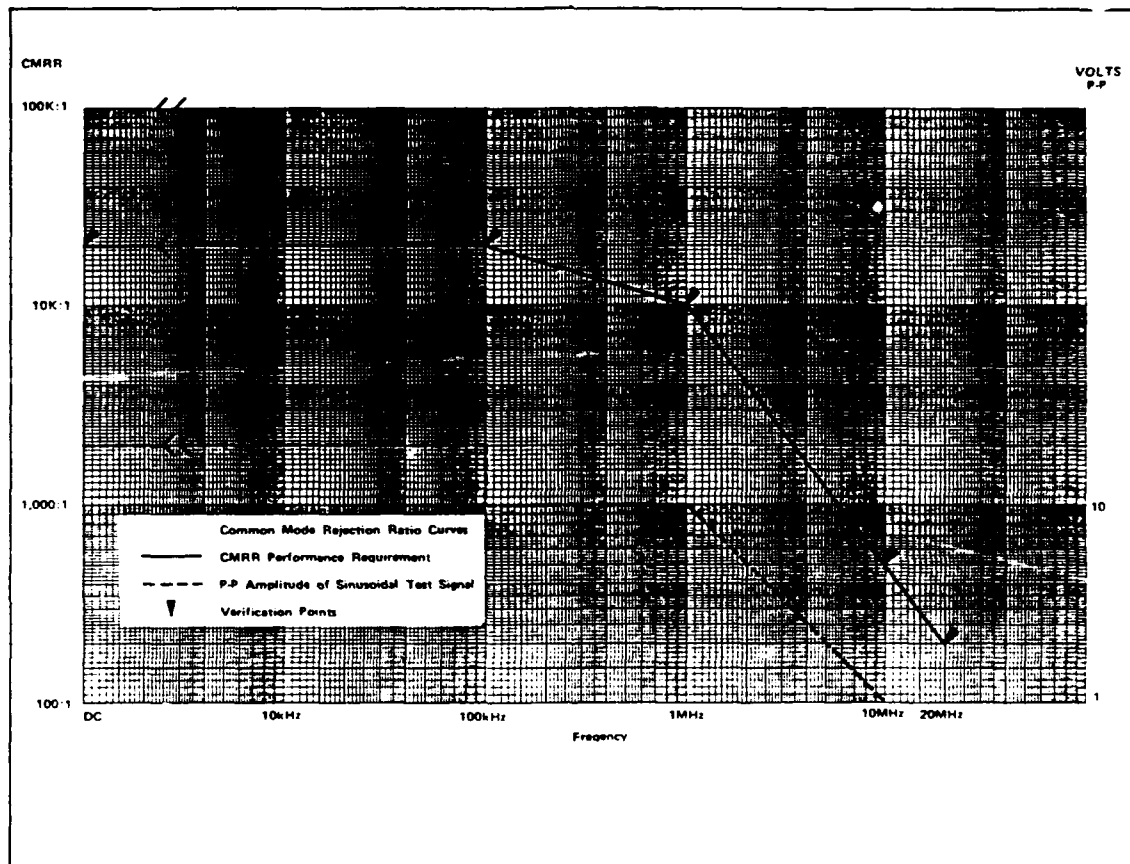


Figure 6.15 Common Mode Rejection Ratio of the 7A13 Differential Amplifier  
[Ref. 17:pp. 1-3]

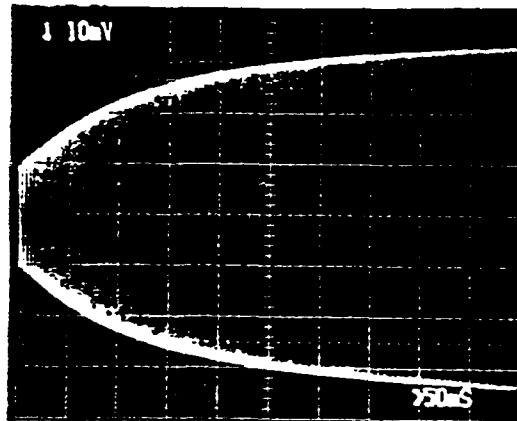


Figure 6.16a Frequency Response of the Differential Data Link  
between 200 Hz and 4.4 KHz

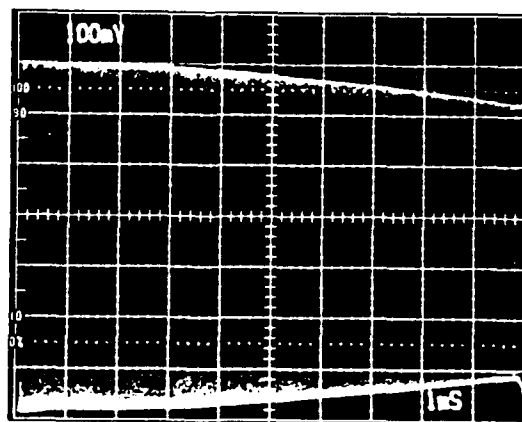


Figure 6.16b Frequency Response of the Differential Data Link  
between 200 KHz and 20 MHz

Figure 6.17a shows the response of the data link to a  $0.35 V_{pp}$  common mode input sweeping from 200 kHz to 20 MHz. For frequencies below 200 kHz the response is approximately zero, indicative of a CMRR approaching that of the 7A13 differential amplifier. Above 200 kHz, the response grows at a uniform rate, indicative of a rapidly deteriorating CMRR. This is to be expected, since the velocity of propagation is not equal in the two cables, which causes a phase difference between their respective signals. This phase difference becomes more pronounced for higher frequencies since their wavelengths decrease with respect to the fixed length of the data link (20 meters). If the frequency were swept even higher, nodes and antinodes would appear on the response due to phase shifts through constructive ( $180^\circ$  phase difference between signals applied to the differential amplifier) and destructive ( $0^\circ$  phase difference) alignment.

The phase shifts just described will cause an incomplete cancellation of the common-mode signal in the differential amplifier, which in turn decreases the CMRR. The decrease in the CMRR will reduce the immunity of the data link to radiated noise power produced by the FXR generator. Fortunately, the phase shift can be corrected easily by the installation of incremental transmission line segments on the cable that displays the lesser phase shift.

The installation of incremental transmission line segments will cause an additional phase shift in the cable on which they are installed by introducing a small amount of time delay. The simplest method of accomplishing this is to use BNC couplers as incremental transmission line segments. Each male/female coupler assembly adds approximately 3 centimeters of length to a cable when installed.

Figure 6.17b shows the response of the data link when two male and two female BNC couplers are installed on the cable with the lesser phase delay. Note that a dramatic improvement in the CMRR is achieved by this simple procedure. This has proven to be the optimum arrangement for obtaining a satisfactory CMRR on this data link.

Using the method for determining CMRR previously alluded to, the worst case value between 200 kHz and 20 MHz is approximately 290 at 3.7 MHz with the BNC couplers installed. It should be noted that the ripple apparent on the response of Figure 6.17 is due to reflections occurring within the coaxial cables due to subtle impedance irregularities along their length, and is not due to the test procedure or the terminating impedances used. These irregularities occur in all transmission lines and can be significantly reduced only by the use of the highest quality, solid conductor, gas-filled coaxial lines. Fortunately, this problem is of little consequence for the data collection configuration used here and should not introduce any significant errors in the collected data.

The shielded target enclosure, shielding arrangement and target alignment apparatus are shown in Figure 6.18. This target assembly arrangement allows the installation of different thicknesses of lead shielding, the changing of the size of the target enclosure and the accurate movement of the target with respect to the aperture in the shield plates. The target may also be rotated by 180° for irradiation of its back side if desired.

The size, shape, material and wall thickness of the target enclosure has been shown to have a significant effect on the IEMP yield of a given target. The arrangement of Figure 6.18 was built to allow the researcher ample means by which to alter the experimental configuration to examine these yield effects in full.

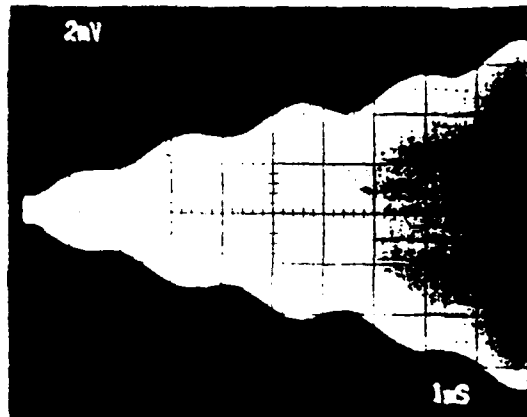


Figure 6.17a Frequency Response of the Differential Data Link between 200 kHz and 20 MHz for a 0.35 V<sub>pp</sub> Signal Applied Common Mode

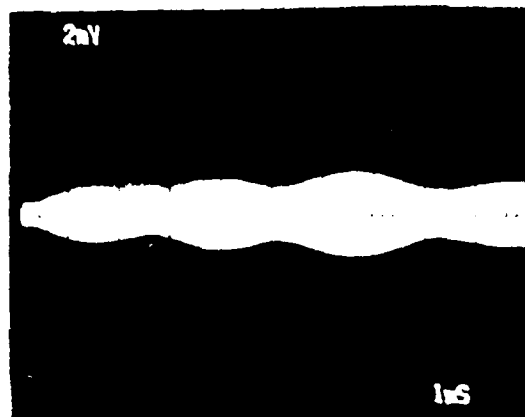


Figure 6.17b Frequency Response of the Differential Data Link between 200 kHz and 20 MHz for a 0.35 V<sub>pp</sub> Signal Applied Common Mode with Optimum Phase Delay Added to One Cable

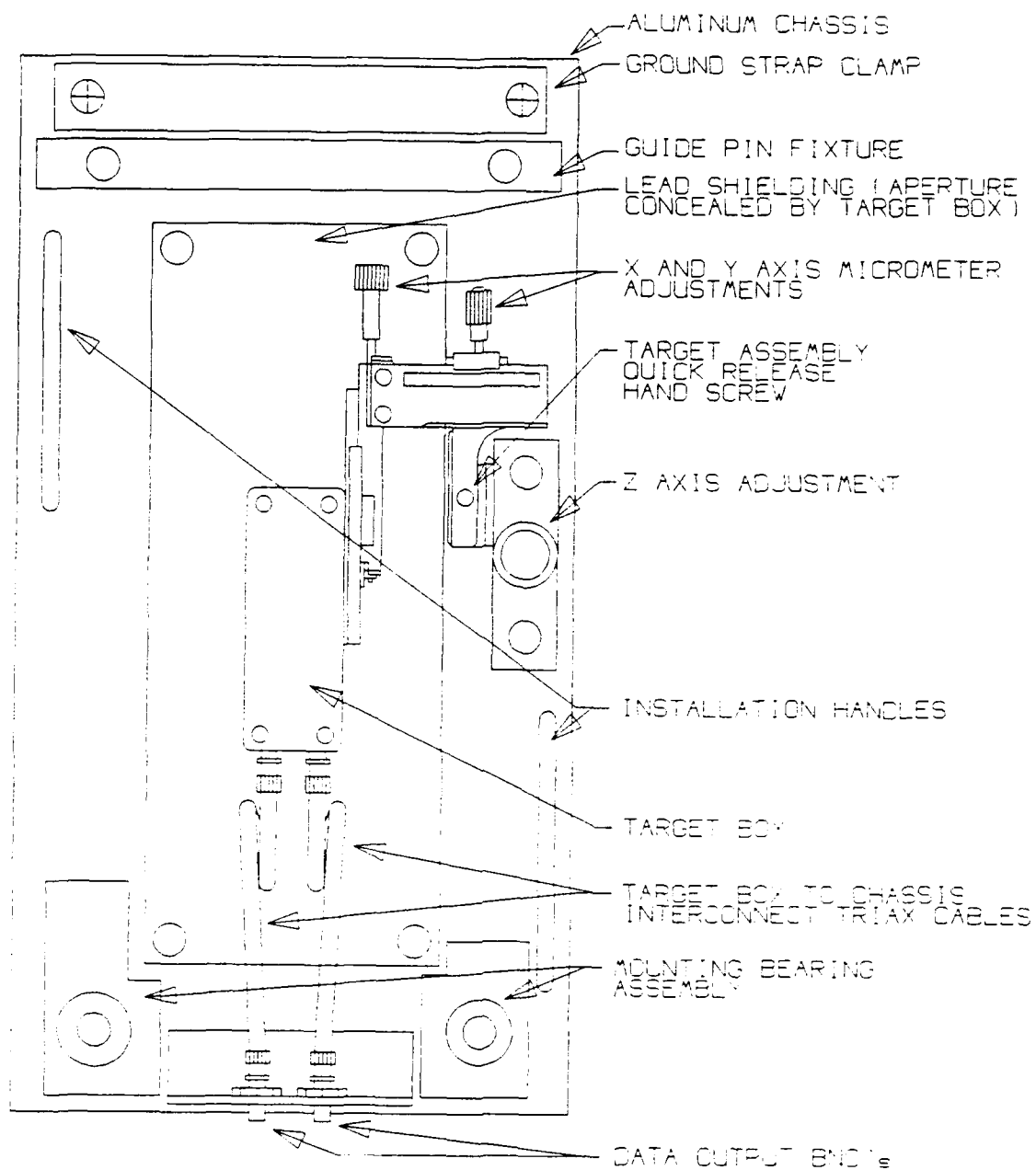


Figure 6.18 Target Assembly for Use with the Differential Data Link

## VII. INTERPRETATION OF RESULTS AND EFFECTS DURING IEMP TESTING

IEMP testing is wrought with uncertainties and aberrations. The random variations in exposure, pulsewidth, emitted beam angle, and EMP emissions makes collection of meaningful data in a FXR facility more voodoo than science. Predictions of quantities of interest are so mediocre that experimentation is often the only useful method to foretell future results.

The ability to differentiate between meaningful data, and that which is altered by the test conditions can only be obtained with hands-on experience. This section will attempt to convey a sufficient amount of experimentally obtained information to allow future researchers to make intelligent choices as to experimental design and data interpretation.

The data collection system depicted in Figure 6.7 will be used exclusively in this discussion. Note that complete information with regard to the characterization and use of all the components of the system is contained in the appendices, as listed in the table of contents.

Many seemingly innocuous mistakes may cause results that launch researchers into quests for irradiation effects that do not exist. A prime example is illustrated in Figure 7.1. This is a photon-induced pulse obtained from the irradiation through a 0.05 cm<sup>2</sup> aperture of the temperature sensor depicted in Figure 2.5. Three distinct pulses appear, one positive and two negative. Only one pulse is meaningful information, while the other two result from the scale factor function of the Tektronix 7104 oscilloscope mainframe. Figure 7.2 depicts a pulse obtained under similar conditions with the scale factor function disabled.



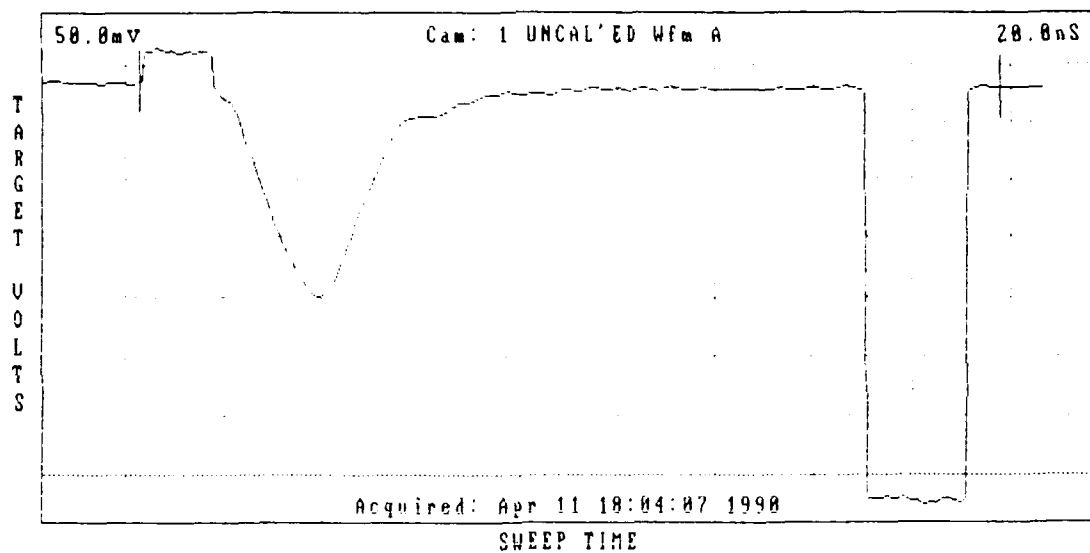


Figure 7.1 Photon-induced Pulse and Two Pulses Caused by Oscilloscope Scale Factors

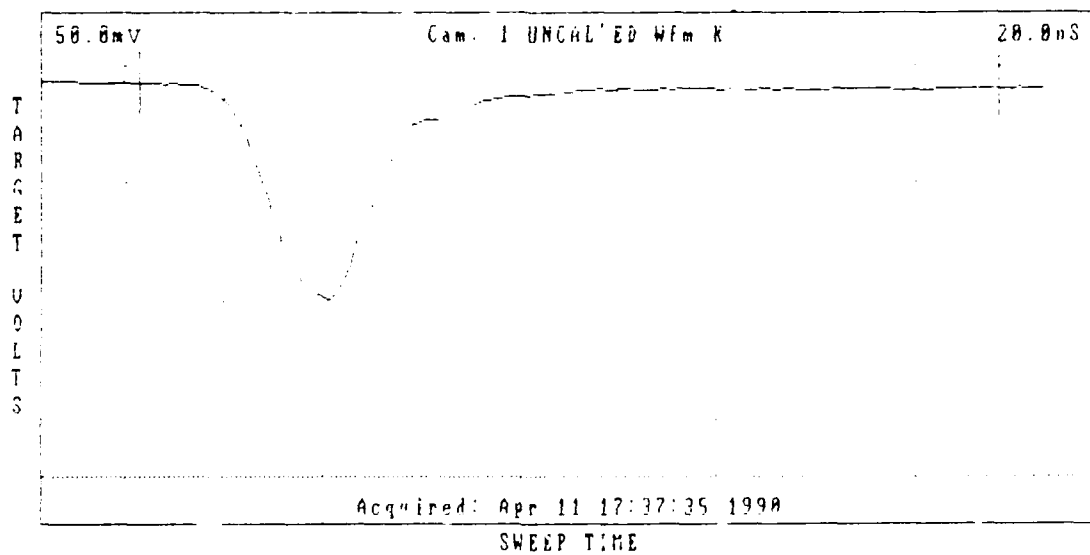


Figure 7.2 Photon-induced Pulse without Scale Factor Corruption

Another blunder is illustrated in Figure 7.3. This positive-going pulse was obtained from the irradiation of a 1 cm<sup>2</sup> brass pad, with the target box rotated 180° to allow irradiation of the opposite face. Unfortunately the differential cables were not exchanged with the rotation, resulting in an output of reversed polarity. It should be noted that the actual photon-induced pulse is positive going, but the negative polarity setup was chosen as the standard to match that used for the Pulserad 112A current characterization and trigger pulses (see Figure 4.2b).

As was alluded to earlier, the shielded box containing the target may have a drastic effect on the yields obtained during irradiation testing. Figure 7.4 displays a pulse obtained from the wafer-scale device using a target shield box with a rear cover approximately one centimeter from the irradiated device. This seemingly normal pulse was shown to be highly attenuated by the effects of the enclosure when compared to a pulse collected under similar conditions, but in a larger box with a distance of 10 centimeters from the target device to the rear cover (Figure 7.5).

The causes of this attenuation are not clear; however, the emission of secondary electrons from the shielded box itself is the likely culprit. As discussed in Section V, the irradiation of the target box as a whole is impossible to prevent, thus it can be expected that a number of characteristics present in collected data can be attributed to the shielded enclosure. Experience has indicated that for enclosures with a distance of eight centimeters or more from the irradiated target to the rear cover, the amplitude distortion to the data will be insignificant, and, in some rare cases, the rear cover may be left off all together with only minor levels of EMP noise introduced to the IEMP data.

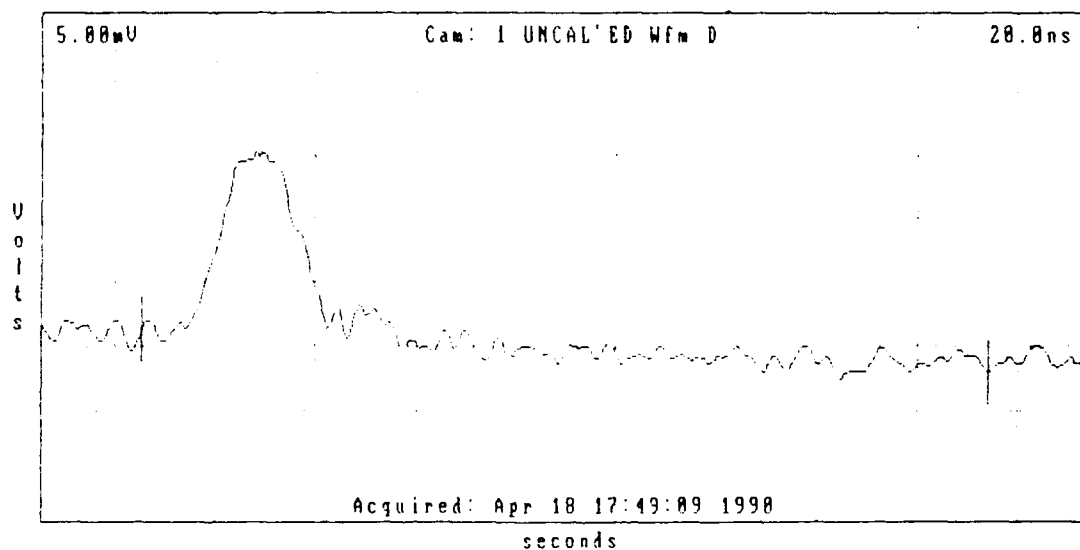


Figure 7.3 Photon-Induced Pulse with Differential Data Link Cables Reversed

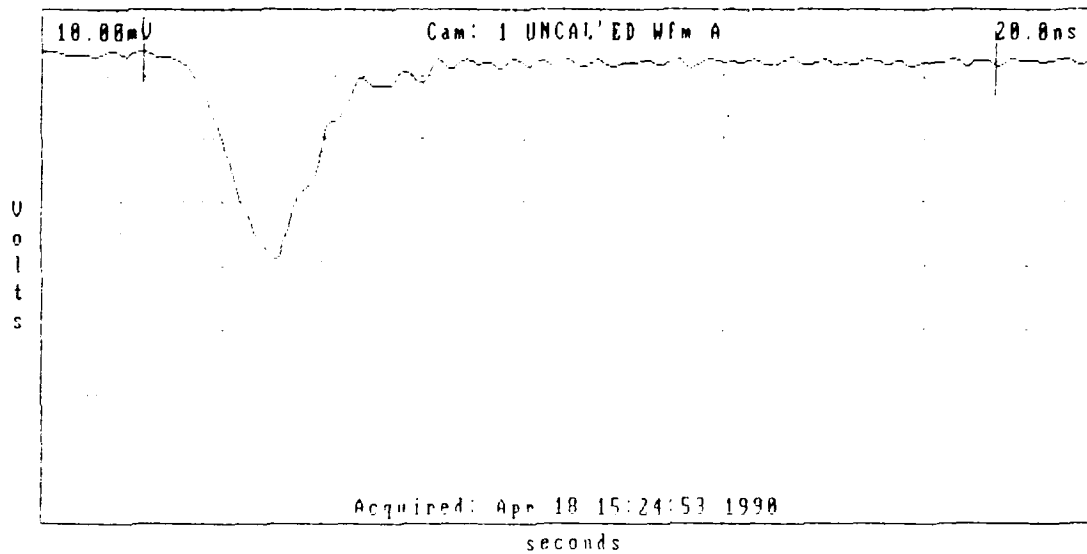


Figure 7.4 Photon-Induced Pulse from a 1 cm<sup>2</sup> Brass Pad  
inside a Small Target Shield Box

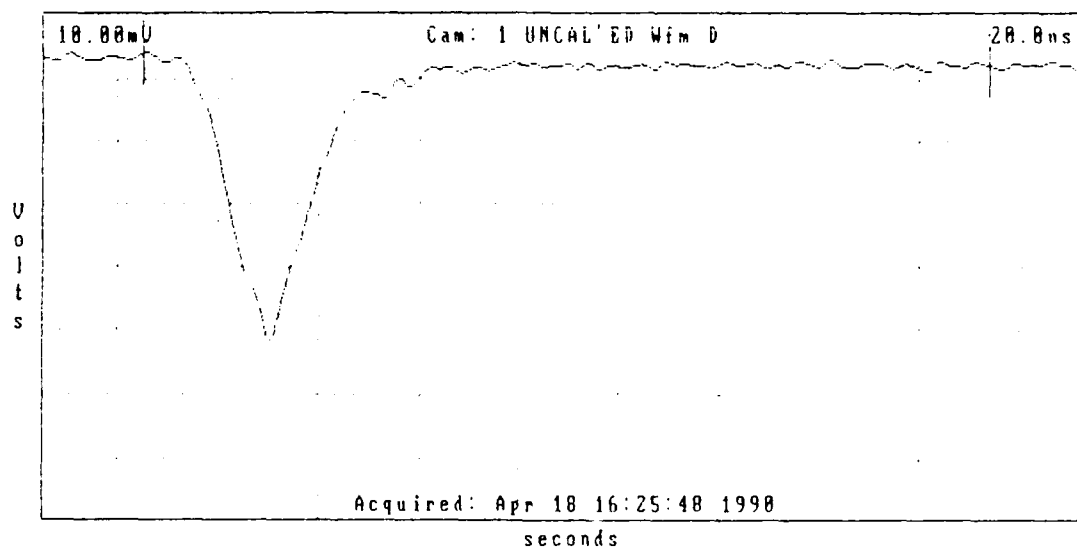


Figure 7.5 Photon-Induced Pulse from a 1 cm<sup>2</sup> Brass Pad  
inside a Large Target Shield Box

As a final note, it is likely that the front cover of the target will cause similar amplitude distortion to the data. Unfortunately the distance from the target to this cover cannot be increased, since this would cause a drastic decrease in the X-ray exposure (see Figure 5.4). To deduce the secondary electron yield from the front cover, it should be made as thin as possible. A thin target will produce less secondary electrons due to the fewer Compton interactions that take place. Note that the front cover must always be installed to prevent severe EMP pickup (Figure 7.6).

#### **A. DIFFERENTIATING BETWEEN PHOTON EFFECTS AND EMP EFFECTS**

In many cases the effects of EMP may overshadow or modify the results of a given irradiation test. It is therefore useful to have a method of isolating the effects of IEMP from those of the induced EMP when questions arise as to the source of a particular response. Several methods were investigated and one has proven to be useful for most target applications.

As indicated previously, different materials will yield different quantities of secondary electrons when irradiated with a spectrum of photons. Electrical conductors generally provide high yields, while insulators generate few free electrons under X-ray irradiation. Most insulators also possess the ability to trap or deflect free electrons injected into them, depending on the properties of the insulating material. These properties can be used to separate the effects of EMP and IEMP at the target under test.

Figure 7.7 shows the yield of a brass pad being irradiated with 3.5 R total dose. This same target then was covered on both sides with silicon vacuum grease (this grease is used extensively for lubricating seals on the FXR generator and thus is readily available) and radiated under the same conditions (Figure 7.8). It can be

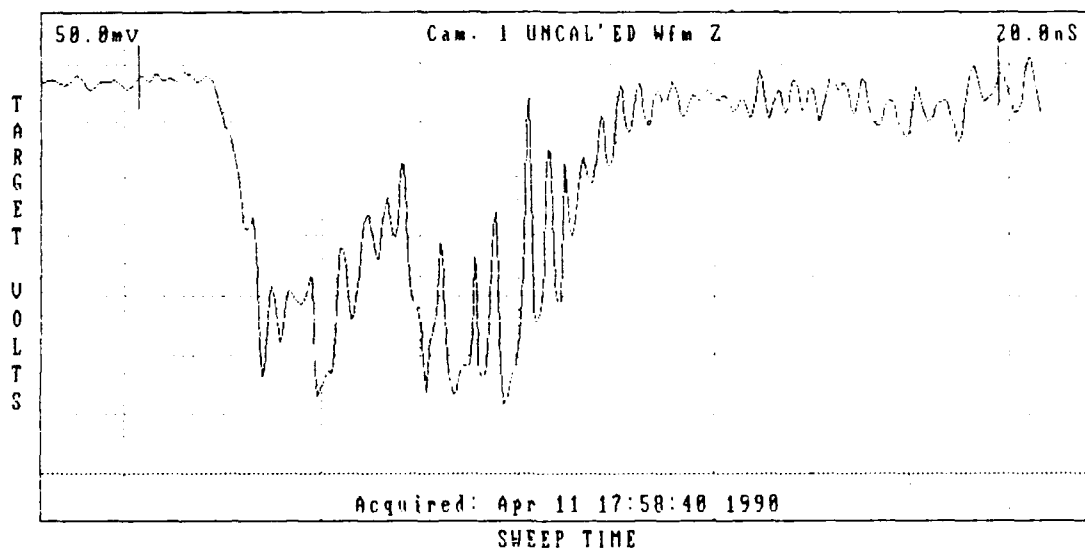


Figure 7.6 Severe EMP Pickup Caused by the Removal of the Front Cover from the Target Shield Box. The experimental conditions are identical to that of Fig. 7.5, except the target box front cover has been removed.



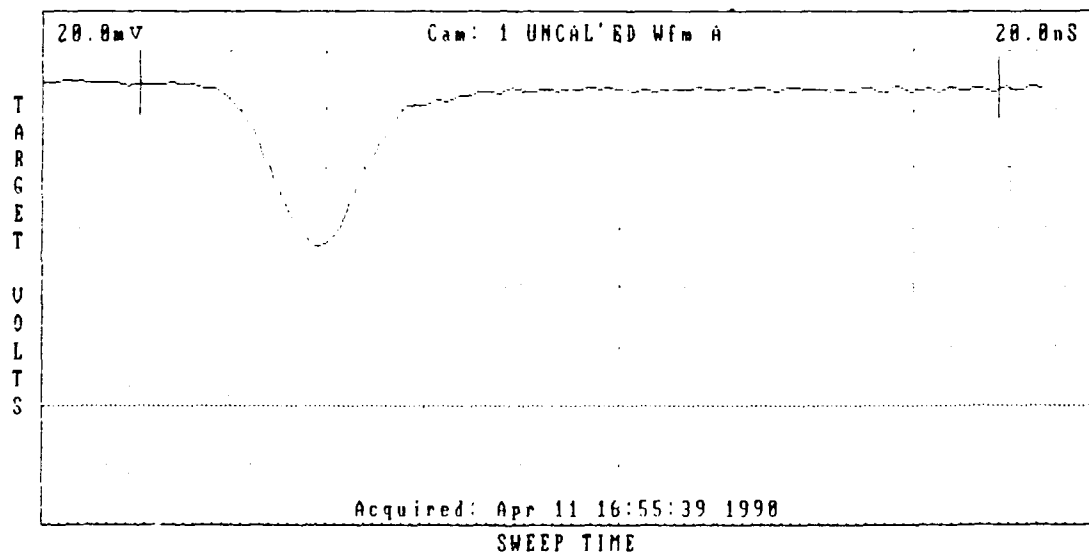


Figure 7.7 Photon Irradiation of a 1 cm<sup>2</sup> Brass Pad

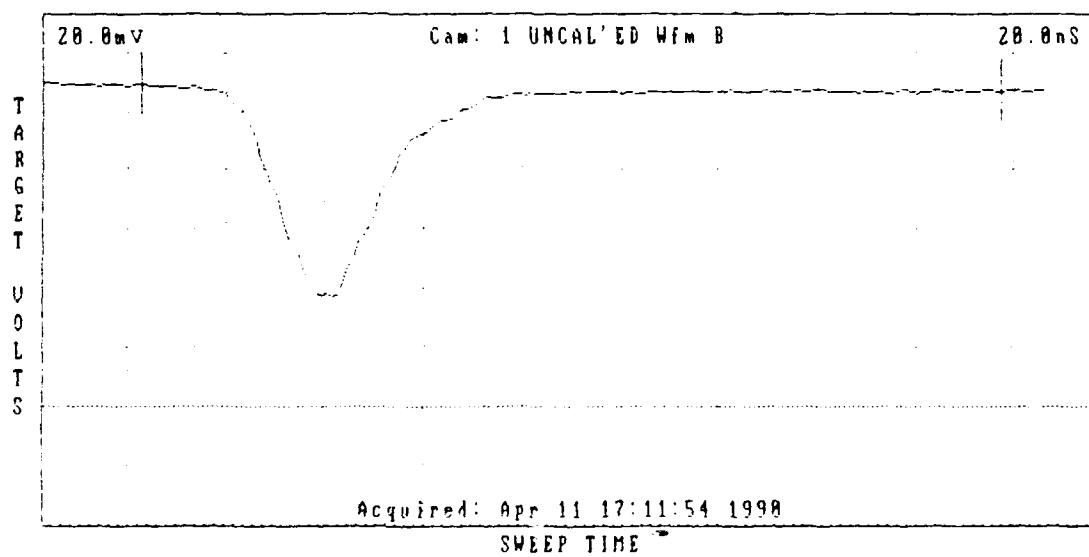


Figure 7.8 Photon Irradiation of a 1 cm<sup>2</sup> Brass Pad Covered with Silicon Grease

seen that the pulse amplitude has increased measurably from the previous case of Figure 7.7.

Although the exact mechanisms responsible for this increase are difficult to predict or ascertain, it has been shown over many separate instances with varying target configurations to consistently provide greater yields than the case of a target free from insulating grease. Since there are no convincing arguments to suggest that this yield increase could be caused by EMP, it may be safely assumed that the pulse is due primarily to photon interactions with the target.

In many cases, the photon-induced current yield of a device under test will vary drastically depending upon its attitude during irradiation. Figure 7.9 illustrated the yield of the wafer scale temperature sensor being irradiated through its aluminum mounting case. In this configuration the X-rays pass through the aluminum case and silicon substrate before striking the gold traces (Figure 2.5). Figure 7.10 shows the yield of the same device when irradiated from the opposite direction. Here the X-rays pass through the plastic face of the mounting case before striking the gold traces and silicon substrate.

The dramatic yield differences noted here are due to the Compton effects of the different materials involved, as well as their relationships to one another, and cannot be attributed to EMP. Thus the careful alteration of the sample attitude is useful as a means to isolate EMP from IEMP in a target during initial experimental setup and design.

#### **B. REDUCTION OF PHOTON EFFECTS OF EXTRANEEOUS OBJECTS DURING IEMP TESTING**

It was pointed out in Section V that the dose through 0.05 cm<sup>2</sup> aperture in a one inch lead plate was only twice that obtained through the lead directly. The

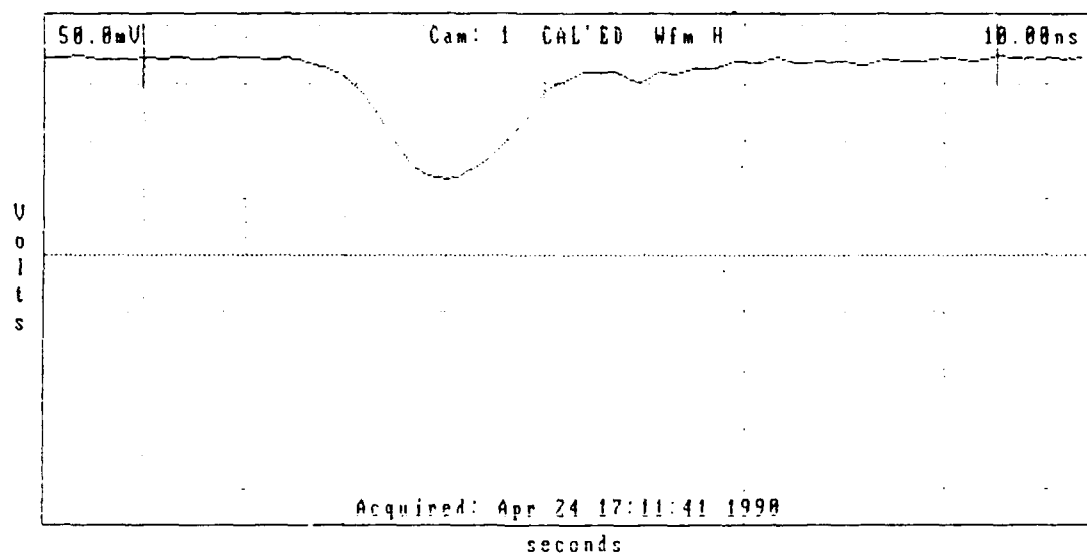


Figure 7.9 Photon Irradiation of a Wafer Scale Temperature Sensor through its Aluminum Case and Silicon Substrate

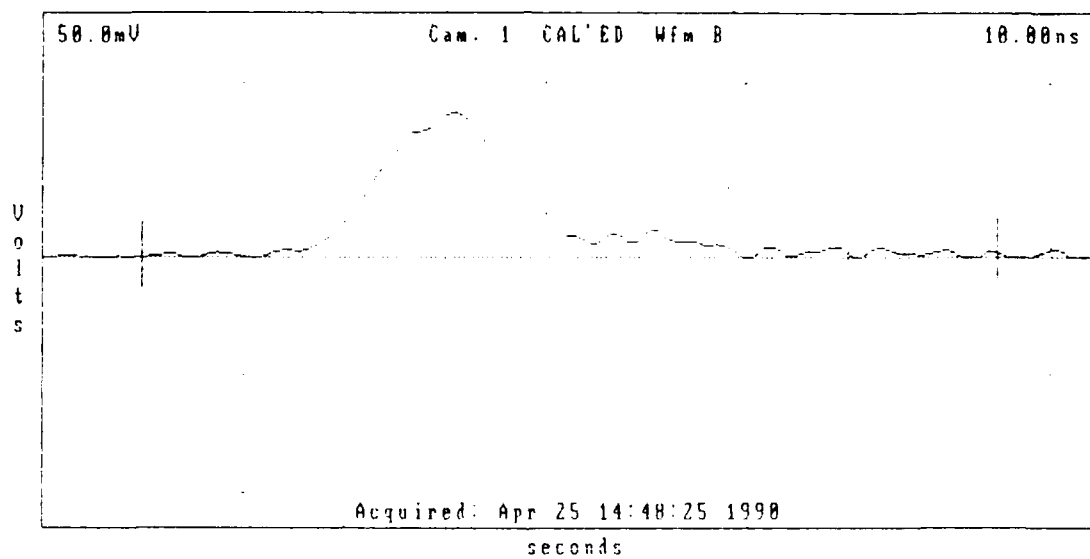


Figure 7.10 Photon Irradiation of a Wafer Scale Temperature Sensor through its Plastic Face

X-rays penetrating the shielding may have an adverse effect on data collection, since some components will invariably be irradiated by this undesirable radiation.

Predicting the effects of this leakage radiation is next to impossible. The irradiation of wires, printed circuit board traces, balun transformers, connector pins, et cetera, all produce a yield, depending upon the dose received, attitude, and numerous other factors. However, the effects of leakage radiation on extraneous objects can be greatly reduced by following simple procedures when collection and processing the data.

Referring to Figure 6.7, it can be seen that the data displayed on the Tektronix 7104 oscilloscope is recorded by the use of a Tektronix C1001 digitizing camera system (DCS). This system digitizes the information presented on the screen of the oscilloscope and processes it in a format that is compatible with disk operating system (DOS) computers.

The DCS software has a number of useful functions that can be utilized to improve data accuracy.

The pulses from several shots may be averaged using the ADD and SCALE functions within the WFM—OPS menu of the DCS (see the DCS operations manual [Ref. 18] and the appendix for complete information on use of the DCS software). The basic operation is:

$$(A + B) \times (0.5) = C \quad (7.1)$$

where

A = first data pulse to be averaged,

B = second data pulse to be averaged, and

C = arithmetic average of A and B.

This procedure may be repeated with numerous waveforms to obtain a pulse that is generally representative of a given sample for a given set of FXR generator parameters. Care should be taken to make sure that all the samples are equally weighted when taking an average. This can be assured if the number of samples taken satisfies the following relationship:

$$N = 2^M \quad (7.2)$$

where,  $N$  = number of data waveforms taken and  $M$  = any positive integer.

Using a number of sample pulses that satisfies the above relationship, the averaging arrangement of Figure 7.11 can be used to overcome the limitation of two waveforms per calculation that is imposed by the DCS software. It should be noted that the AVERAGE function within the ACQUIRE menu should not be used, since the overall data average may be corrupted by one or more mis-firings during a series of FXR generator shots.

Figure 7.12 shows an averaged pulse obtained by irradiation of the temperature sensor of Figure 2.5. This pulse is the average of 4 pulses and was irradiated with an average dose of approximately 5 R.

To remove the signal added to this by the yields of other components in the target test box, the temperature sensor was removed, the empty target box was irradiated, and the resulting yields were measured and averaged under identical conditions. This pulse is displayed in Figure 7.13.

To remove the box yield from the total, the DCS SUBTRACT function within the WFM-OPS menu was used. Figure 7.14 shows the average target yield less the test box yield. This represents a close approximation to the actual yield of the target alone. Note that no aperture was used in the lead shield for this procedure,

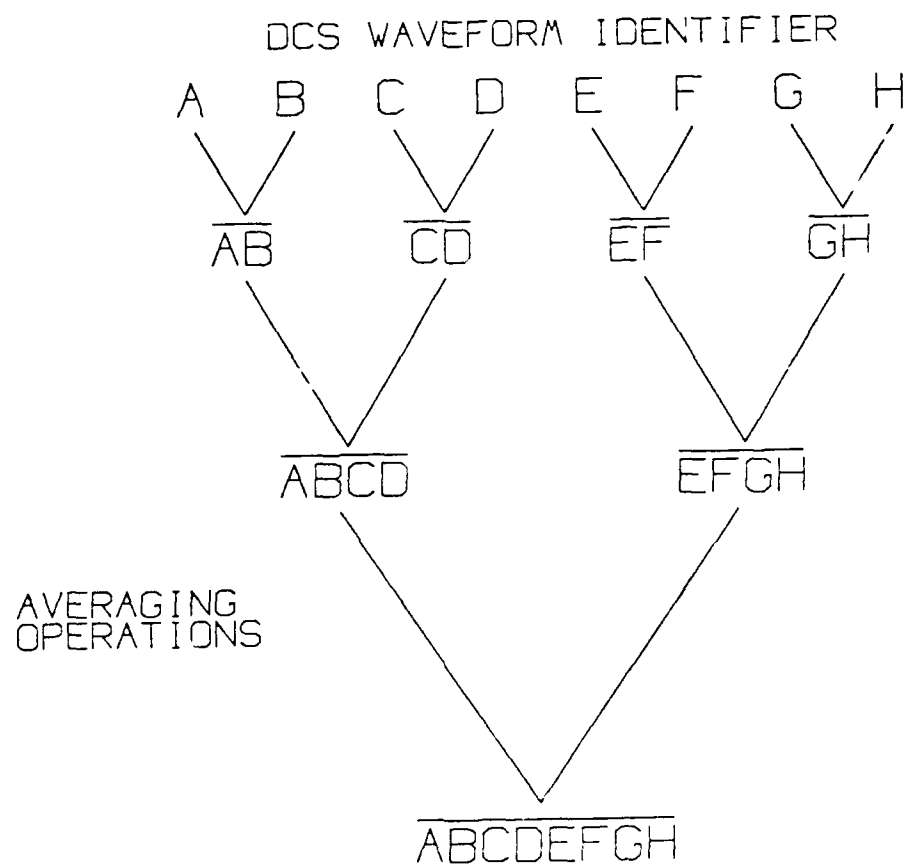


Figure 7.11 Equal Weighted Averaging of N Sample Waveforms



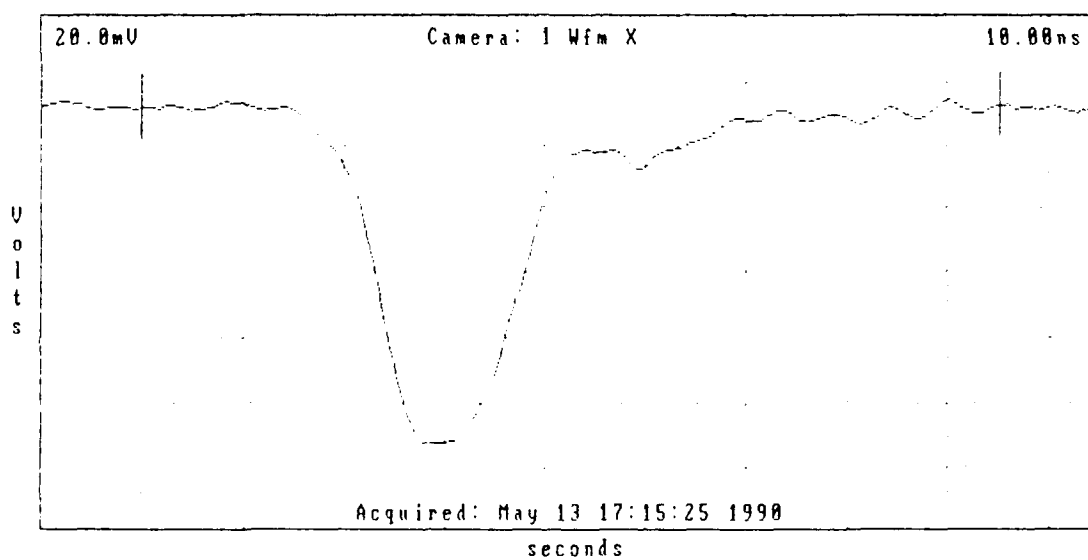


Figure 7.12 Average Yield of Wafer-Scale Temperature Sensor and Extraneous Components When Radiated with an Average Dose of 5 R

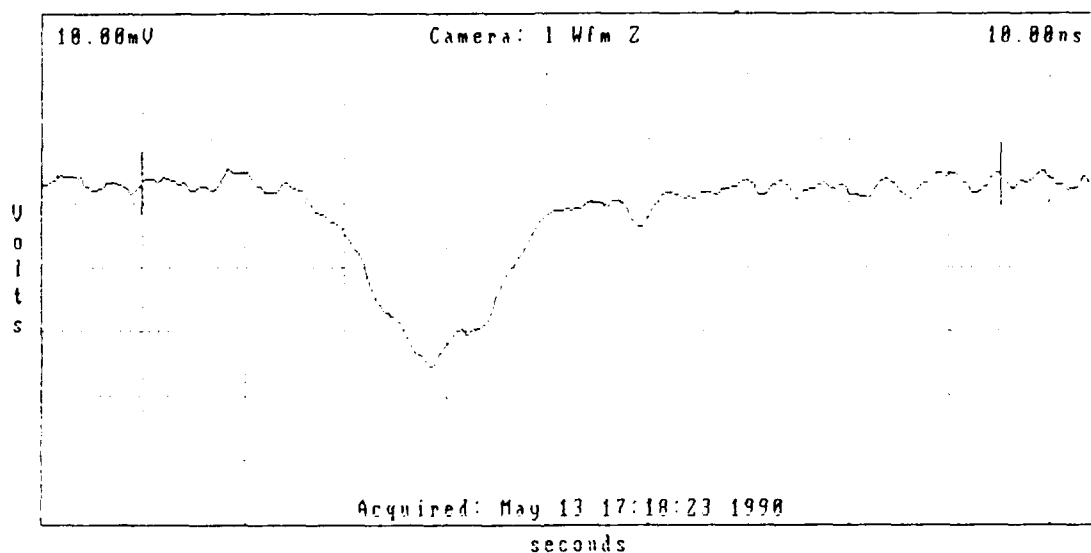


Figure 7.13 Average Yield of Empty Target Shield Box When Radiated with an Average Dose of 5 R

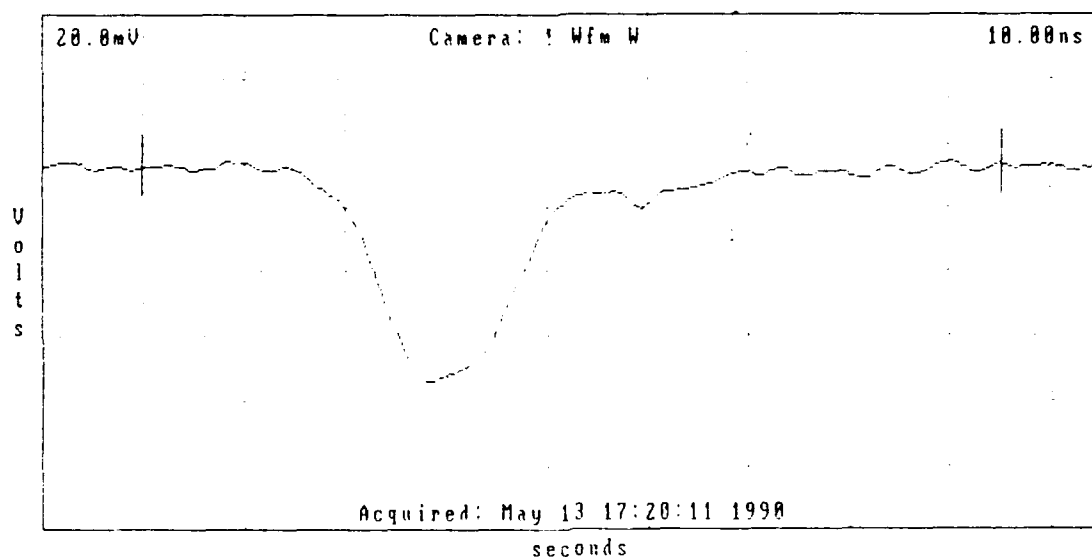


Fig. 7.14 Average Yield of Wafer-Scale Temperature Sensor with the Yield Effects of Extraneous Components Subtracted

since the use of an aperture as an X-ray directive means has proven to be ineffective, and the target consists of five individual 1 cm<sup>2</sup> sensors internally wired in parallel. Thus the yield of one sensor is approximated by dividing the total yield by 5 and using the average dose of 5 R.

Note that the procedure just described has the effect of providing an artificial aperture for the target area of interest, since the cancellation of all signals contributed by components other than the intended target mimics the function of an ideal aperture. For this reason, it is recommended that this procedure be used whenever possible for data collection at the NPS FXR facility in lieu of a physical aperture, or as a supplement to improve the fidelity of the data when a physical aperture structure is deemed mandatory.

## VIII. CONCLUSIONS AND RECOMMENDATIONS

The photon irradiation in the NPS FXR facility of small electronic components in general, and wafer-scale integrated devices in particular can yield useful data only when careful attention is paid to the details of data collection techniques and their implementation. Considerable time can be wasted and important data lost if due care is not exercised with regard to experimental layout and design.

Since the techniques used in this study have proven to be effective in producing valid TREE data, it is advisable that they be followed wherever possible, or at least used as a starting point for the design of specialized instrumentation for future experiments.

In particular, the information presented in Section VII should be referenced when data is being collected. It is imperative that researchers learn to recognize and compensate for the numerous error sources present in the FXR facility. It is advisable that all instrumentation systems be tested under known conditions (the irradiation of a 1 cm<sup>2</sup> pad is a standard yield test source) before attempting to collect data on an actual sample of interest.

## APPENDIX A

### CHARACTERIZATION OF NPS FXR DATA LINK

The following procedures can be used to obtain characterization information on the differential data link described in this thesis.

#### A. OBTAINING FREQUENCY RESPONSE CURVES

##### 1. Required Equipment

- a. HP3314A Sweep Generator (or equivalent)
- b. TEK C-50 Oscilloscope Camera (or equivalent)
- c. TEK 7104 Oscilloscope (or equivalent)
- d. TEK 7A12 Differential Comparator Plug In
- e. TEK 7B92A Horizontal Time Base Plug In (or equivalent)
- f.  $50\Omega$ , .25W, 1% Resistor
- g.  $50\Omega$  coaxial cable assembly three feet long with a BNC connector on one end and two mini alligator clips on the other
- h.  $50\Omega$  coaxial cable from the radiation area to the RFI enclosure

##### 2. Equipment Setup (Refer to Appropriate Operator's Manual)

- a. HP3314A
  - (1) AMPTD: 70 mV
  - (2) SWEEP: LIN
  - (3) SW/TR INTVL: 10 ms
  - (4) START FREQ: 199 kHz (for high frequency sweep)
  - (5) STOP FREQ: 19.99 MHz (for high frequency sweep)
  - (6) FUNCTION: SINE
  - (7) GEN: FREE RUN
  - (8) TRIGGER: INT

- b. TEK C-50 Oscilloscope camera (suggested setting when using Polaroid 667 film)
  - (1) APERTURE: 2.8
  - (2) SHUTTER SPEED: T5
  - (3) MODE: NORM
  - (4) FOCUS: As required
- c. TEK 7104 Oscilloscope
  - (1) VERTICAL MODE: LEFT (TEK 7A13 installed in left slot)
  - (2) HORIZONTAL MODE: B (TEK 7B92A installed in right slot)
  - (3) TRIGGER MODE: LEFT VERTICAL
  - (4) INTENSITY: Approx. 30% of full
  - (5) GRAT ILLUM: PULSED
  - (6) + GATE/EXT (of grat illum): + GATE
  - (7) READOUT: PULSED
  - (8) + GATE/EXT (of readout): + GATE
  - (9) All Other Controls Not Used
- d. TEK 7A13 Differential Comparator Plug In
  - (1) VERTICAL SENSITIVITY: 10 mV/div
  - (2) CHANNEL ONE SOURCE: D.C.
  - (3) CHANNEL TWO SOURCE: D.C.
  - (4) BANDWIDTH: FULL
  - (5) POSITION: Trace on center of screen (initial position)
  - (6) VARIABLE BALANCE: Centered
  - (7) All Other Controls Not Used

- e. TEK 7B92A Horizontal Time Base Plug In
  - (1) HORIZONTAL SWEEP TIME: 1 ms/div
  - (2) TRIGGER SWEEP TIME: EXTERNAL
  - (3) TRIGGER LEVEL: Approx. zero (adjust for steady display)
  - (4) TRIGGER COUPLING: A.C.
  - (5) TRIGGER MODE: AUTO
  - (6) SLOPE: +
  - (7) COUPLING: A.C.
  - (8) SOURCE: EXTERNAL
  - (9) EXTERNAL TRIGGER IMPEDANCE: 50 $\Omega$
  - (10) All Other Controls Not Used

3. Upper Bandwidth (200 kHz to 20 MHz) Characterization Procedures  
(Refer to Figure A.1)

- a. Remove the target from the target shield box
- b. Remove the target load resistor from its socket in the target shield box
- c. Connect the output of the HP3314A through the 50 $\Omega$  resistor to the ungrounded socket of the target load resistor socket with the 50 $\Omega$  coaxial cable. Ground the cable shield to the target box
- d. Connect a 50 $\Omega$  coaxial cable between the HP3314A trigger output and the TEK 7B92A trigger input
- e. Adjust the horizontal position on the TEK 7B92A plug-in so that the trace starts on the left margin of the screen



- f. Photograph the display using the TEK C-50 oscilloscope camera (some camera settings may need to be changed to acquire an acceptable photograph).
- g. To characterize the lower bandwidth (400 Hz to 4.4 kHz), change the start and stop settings on the HP3314A to 400 Hz and 4.4 kHz respectively and repeat the above procedure.

## **B. OBTAINING COMMON MODE REJECTION RATIO CURVES**

### **1. Required Equipment**

- a. HP3314A Sweep Generator (or equivalent)
- b. TEK C-50 Oscilloscope Camera (or equivalent)
- c. TEK 7104 Oscilloscope (or equivalent)
- d. TEK 7A13 Differential Comparator Plug In
- e. TEK 7B92A Horizontal Time Base Plug In (or equivalent)
- f. 3 foot long 50 $\Omega$  coaxial cable with 2 BNC connectors installed on either end
- g. CMRR Cable Test Box (refer to Figure A.2)
- h. 50 $\Omega$  coaxial cable from radiation area to RFI enclosure

### **2. Equipment Setup (Refer to the Appropriate Operator's Manual)**

- a. HP3314A
  - (1) AMPTD: 700 mV
  - (2) SWEEP: LIN
  - (3) SW/TR INTVL: 10 ms
  - (4) START FREQ: 199 kHz
  - (5) STOP FREQ: 19.9 MHz
  - (6) FUNCTION: SINE

- (7) GEN: FREE RUN
- (8) TRIGGER: INT
- b. TEK C-50 Oscilloscope Camera
  - (1) APERTURE: 2.8
  - (2) SHUTTER SPEED: T5
  - (3) MODE: NORM
  - (4) FOCUS: as required
- c. TEK 7104 Oscilloscope
  - (1) VERTICAL MODE: LEFT (TEK 7A13 installed in left slot)
  - (2) HORIZONTAL MODE: B (TEK 7B92A installed in right slot)
  - (3) B TRIGGER SOURCE: LEFT VERTICAL
  - (4) INTENSITY: Approx. 30% of full
  - (5) GRAT ILLUM: PULSED
  - (6) + GATE/EXT (of grat illum): + GATE
  - (7) READOUT: PULSED
  - (8) + GATE/EXT (of readout): + GATE
  - (9) All Other Controls Not Used
- d. TEK 7A13 Differential Comparator Plug In
  - (1) VERTICAL ONE SOURCE: 1 mv/div
  - (2) CHANNEL ONE SOURCE: D.C.
  - (3) CHANNEL TWO SOURCE: D.C.
  - (4) COMPARATOR VOLTAGE: Not used
  - (5) BANDWIDTH: FULL
  - (6) POSITION: Trace on center of screen (initial position)

- (7) VARIABLE BALANCE: Centered
- (8) All Other Controls Not Used
- e. TEK 7B92A Horizontal Time Base Plug In
  - (1) HORIZONTAL SWEEP TIME: 1 ms/div
  - (2) TRIGGER SOURCE: EXTERNAL with positive slope
  - (3) TRIGGER LEVEL: Approx. zero (adjust for steady display)
  - (4) TRIGGER COUPLING: A.C.
  - (5) TRIGGER MODE: AUTO
  - (6) SLOPE: +
  - (7) COUPLING: A.C.
  - (8) SOURCE: EXTERNAL
  - (9) EXTERNAL TRIGGER IMPEDANCE:  $50\Omega$
  - (10) All Other Controls Not Used

**3. Common Mode Rejection Ratio Characterization Procedure (Refer to Figure A.2)**

- a. Remove the two triax cable BNC connectors from the target shield box and install them on the CMRR cable test box output BNC's
- b. Connect a  $50\Omega$  coaxial cable between the HP3314A trigger output and the TEK 7B92A trigger input
- c. Connect a  $50\Omega$  coaxial cable between the HP3314A output and the CMRR cable test box input
- d. Adjust the horizontal position on the TEK 7B92A plug-in so that the trace starts on the left margin of the screen

- e. Photograph the display using the TEK C-50 oscilloscope camera (some camera settings may need to be changed to acquire an acceptable photograph)
- f. The CMRR is obtained (approximately) by dividing the constant 0.7 by the peak-to-peak voltage from the photograph at the frequency of interest

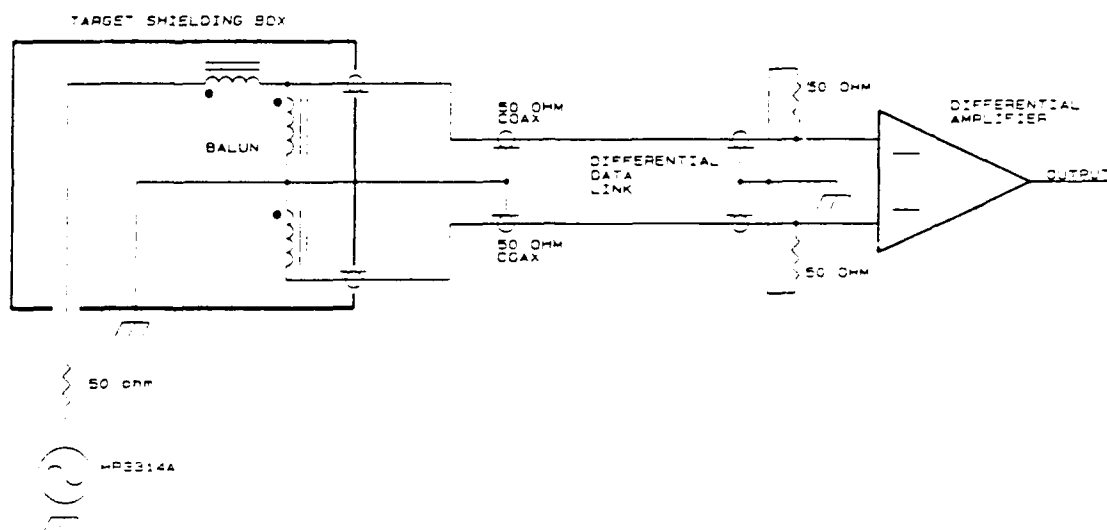


Figure A.1 Schematic Diagram of Bandwidth Characterization Circuitry

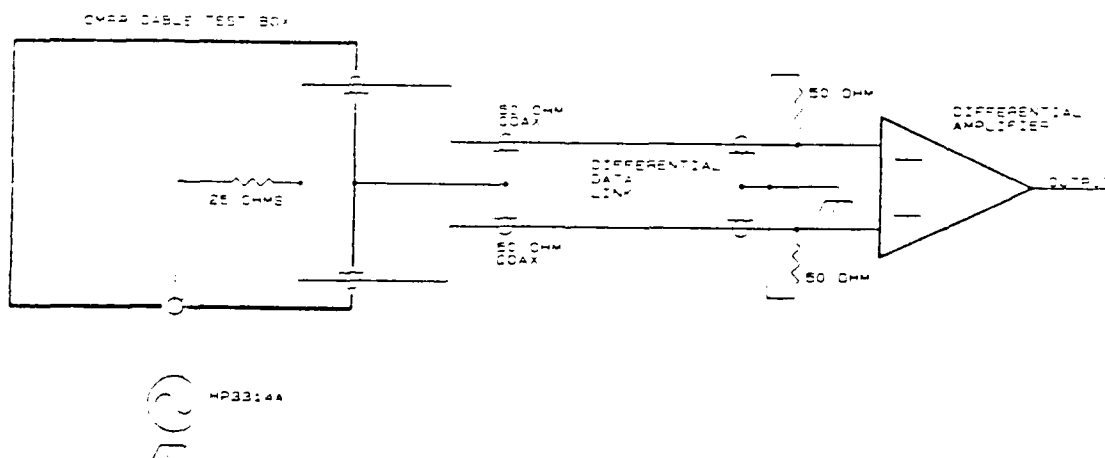


Figure A.2 Schematic Diagram of CMRR Characterization Circuitry

## **APPENDIX B**

### **CONDENSED OPERATING PROCEDURES FOR NPS FXR DIFFERENTIAL DATA LINK**

#### **A. REQUIRED EQUIPMENT**

1. TEK 7104 Oscilloscope (or equivalent)
2. TEK 7A13 Differential Comparator Plug In
3. TEK 7B92A Horizontal Time Base Plug In (or equivalent)
4. TEK C1001 Digitizing Camera System

#### **B. EQUIPMENT SETUP (Refer to Appropriate Operator's Manual)**

1. TEK 7104
  - a. VERTICAL MODE: LEFT (TEK 7A13 installed in left slot)
  - b. HORIZONTAL MODE: B (TEK 7B92A installed in right slot)
  - c. B TRIGGER SOURCE: RIGHT VERTICAL
  - d. INTENSITY: Full clockwise
  - e. All Other Controls Off
2. TEK 7A13
  - a. VERTICAL SENSITIVITY: Usually 10 mV/div, or as required
  - b. CHANNEL ONE SOURCE: D.C.
  - c. CHANNEL TWO SOURCE: D.C.
  - d. BANDWIDTH: FULL
  - e. POSITION: Start at center of screen, change as required
  - f. VARIABLE BALANCE: Centered
  - g. All Other Controls Not used

### **3. TEK 7B92A**

- a. HORIZONTAL SWEEP TIME: 10 ns or as required
- b. TRIGGER SOURCE: EXTERNAL
- c. TRIGGER LEVEL: Approx. zero (change as required)
- d. TRIGGER COUPLING: A.C.
- e. TRIGGER MODE: NORM
- f. SLOPE: NEGATIVE
- g. COUPLING: A.C.
- h. SOURCE: EXTERNAL
- i. EXTERNAL TRIGGERING IMPEDANCE:  $50\Omega$
- j. Other Controls Not Used

### **4. TEK C1001**

- a. Calibrate according to procedure in operator's manual

## **C. COLLECTION OF PHOTON YIELD DATA FROM IRRADIATION OF WAFER SCALE DEVICE**

- 1. Install differential data link cables onto target shield box, making sure labels on cable match those on box (A to A, B to B). Position the target in front of the FXR generator as required.
- 2. Install other end of differential data link cables onto TEK 7104 with A on channel 1, B on channel 2.
- 3. Select LIGHT TRIG under the ACQUIRE menu and toggle to ON. Alternately, the EXT.TRIG function under the ACQUIRE menu can be selected in lieu of the LIGHT TRIG function. This requires the connection of a cable between the + GATE output of the TEK 7104 and the trigger input of the DCS circuit board (see DCS manual for details).

4. Select CALIBRATE under ACQUIRE menu and toggle ON.
5. Press the F1 function key. The screen will display "Waiting for light trigger" or "Waiting for External Trigger(s)", depending on the triggering method selected in part 3 above. This signifies that the system is ready to collect data.
6. Setup and fire the Pulserad FXR generator following the procedure in the operator's manual.
7. The DCS will acquire and display the collected data waveform.
8. Adjust triggering, sensitivity and sweep time as required for an acceptable display. Do not change triggering after an acceptable display is achieved, since this will cause a horizontal displacement in the data which will introduce errors in the data if two waveforms are acted upon by functions in the WFM-OPS menu.
9. After an acceptable display is achieved, repeat steps 5 through 7 to acquire as many waveforms as desired.



## LIST OF REFERENCES

1. Lawrence Livermore National Laboratory Internal Document UCRL-53878-88, *Laser Pantography*, by D. B. Tuckerman, Section I, 1987.
2. Tuckerman, D. B., "Laser - Patterned Interconnects for Thin-Film Hybrid Wafer-Scale Circuits," *IEEE Electron Device Letters*, v. EDL-8, no. 11, p. 5, November 1987.
3. Lawrence Livermore National Laboratory Internal Document UCRL-53878-88, *The VHS1 Ten Chip Memory Hybrid*, by A. T. Barfknecht and J. L. Kashchmitter, Section 1.3, 1987.
4. U.S. Department of Defense and the Energy Research and Development Administration, *The Effects of Nuclear Weapons*, by S. Glasstone and P. J. Dolan, Government Printing Office, Washington, DC, 1977.
5. Rudie, N. J., *Principles and Techniques of Radiation Hardening*, Vol. 1, Western Periodicals Company, 1986.
6. Gnose, R. N., *EMP Environment and Systems Hardness Design*, Interference Control Technologies, Inc., 1984.
7. *McGraw-Hill Encyclopedia of Physics*, 5th ed., McGraw-Hill Book Company, 1982.
8. Passenheim, B. C., *How to do Radiation Tests*, Ingenuity Ink, 1988.
9. Woehler, K. E., *Electromagnetic Pulse Phenomena from Nuclear Explosions, Part IV*, Instructional Notes for NPS Curricula, February 1984.
10. Pietruska, R. B., *Operation and Characteristics of the Flash X-ray Generator at the Naval Postgraduate School*, Master's Thesis, Naval Postgraduate School, Monterey, California, June 1989.
11. Physics International Corporation, Pulsar Products Division, *Model 112A Pulserad Pulsed X-ray Generator Operations and Maintenance Manual*, 1986.
12. Demaw, M. F., *Ferromagnetic Core Design and Applications Handbook*, Prentice Hall, Inc., 1981.
13. Amidon Associates, Inc., *Iron-Powder and Ferrite Coilforms*, 1986.
14. Tipler, P. A., *Physics*, 2nd ed., Worth Publishers, Inc., 1982.
15. Hoyt, W. Jr., *Engineering Electromagnetics*, 4th ed., McGraw-Hill Book Company, 1981.
16. McLyman, W. T., Colonel, *Transformer and Inductor Design Handbook*, 2nd ed., 1988.

17. Tektronix, Inc., *Tektronix 7A18 Differential Comparator Instruction Manual*, 1985.
18. Tektronix, Inc., *Digitizing Camera System Operating Manual*, 1988.

## INITIAL DISTRIBUTION LIST

		No. Copies
1.	Defense Technical Information Center Cameron Station Alexandria, VA 22304-6145	2
2.	Library, Code 0142 Naval Postgraduate School Monterey, CA 93943-5002	2
3.	Mr. Herb Bracewell, Jr. 11 Gillespie Lane Monterey, CA 93940	1
4.	Chairman, Code EC Department of Electrical and Computer Engineering Naval Postgraduate School Monterey, CA 93943-5000	1
5.	Dr. S. N. Michael, Code EC/Mi Department of Electrical and Computer Engineering Naval Postgraduate School Monterey, CA 93943-5000	1
6.	Dr. R. W. Adler, Code EC/Ab Department of Electrical and Computer Engineering Naval Postgraduate School Monterey, CA 93943-5000	1
7.	Dr. K. E. Woehler, Code PH/Wh Department of Physics Naval Postgraduate School Monterey, CA 93943-5000	1
8.	Dr. X. K. Maruyama, Code PH/Mx Department of Physics Naval Postgraduate School Monterey, CA 93943-5000	10

- |     |   |   |
|-----|---|---|
| 9.  | Dr. F. R. Buskirk, Code PH/Bs<br>Department of Physics<br>Naval Postgraduate School<br>Monterey, CA 93943-5000                            | 2 |
| 10. | Dr. J. R. Neighbours, Code PH/Nb<br>Department of Physics<br>Naval Postgraduate School<br>Monterey, CA 93943-5000                         | 2 |
| 11. | Mr. Donald D. Snyder, Code PH<br>Accelerator Laboratory<br>Department of Physics<br>Naval Postgraduate School<br>Monterey, CA 93943-5000  | 1 |
| 12. | Mr. Harold M. Rietdyk, Code PH<br>Accelerator Laboratory<br>Department of Physics<br>Naval Postgraduate School<br>Monterey, CA 93943-5000 | 1 |
| 13. | Physics Library, Code PH<br>Department of Physics<br>Naval Postgraduate School<br>Monterey, CA 93943-5000                                 | 2 |
| 14. | Dr. Nicholas Colella<br>L278<br>Lawrence Livermore National Laboratory<br>P.O. Box 808<br>Livermore, CA 94550                             | 1 |
| 15. | Dr. Joseph Kimbrough<br>L278<br>Lawrence Livermore National Laboratory<br>P.O. Box 808<br>Livermore, CA 94550                             | 1 |
| 16. | Mr. Richard Mendosa<br>Physics International Company<br>P.O. Box 1538<br>San Leandro, CA 94577  | 1 |

- |     |   |   |
|-----|---|---|
| 17. | Mr. Bernie Bernstein<br>Physics International Company<br>P.O. Box 1538<br>San Leandro, CA 94577   | 1 |
| 18. | Mr. Dale Galarowicz<br>Department of Physics, Code PH<br>Naval Postgraduate School<br>Monterey, CA 93943-5000   | 1 |
| 19. | Strategic Systems Program<br>Department of the Navy<br>ATTN: Captain William Bassett<br>Sp-2340<br>Washington, DC 20376                                       | 1 |
| 20. | Dr. William Weddle<br>Guidance Branch<br>Advanced Technology Division<br>Electronic Development Department<br>Naval Weapons Support Center<br>Crane, IN 47522 | 1 |